

The accretion rates and mechanisms of Herbig Ae/Be stars

C. Wichittanakom,^{1,2★} R. D. Oudmaijer,^{2★} J. R. Fairlamb^{lib},³ I. Mendigutía^{lib},⁴
M. Vioque² and K. M. Ababakr⁵

¹Department of Physics, Faculty of Science and Technology, Thammasat University, Rangsit Campus, Pathum Thani 12120, Thailand

²School of Physics and Astronomy, EC Stoner Building, University of Leeds, Leeds LS2 9JT, UK

³Institute for Astronomy, University of Hawaii, 2680 Woodlawn Drive, Honolulu HI 96822, USA

⁴Centro de Astrobiología (CSIC-INTA), Departamento de Astrofísica, ESA-ESAC Campus, PO Box 78, E-28691 Villanueva de la Cañada, Madrid, Spain

⁵Erbil Polytechnic University, Kirkuk Road, 44001, Erbil, Iraq

Accepted 2020 January 7. Received 2020 January 1; in original form 2019 October 9

ABSTRACT

This work presents a spectroscopic study of 163 Herbig Ae/Be stars. Amongst these, we present new data for 30 objects. Stellar parameters such as temperature, reddening, mass, luminosity, and age are homogeneously determined. Mass accretion rates are determined from H α emission line measurements. Our data is complemented with the X-Shooter sample from previous studies and we update results using *Gaia* DR2 parallaxes giving a total of 78 objects with homogeneously determined stellar parameters and mass accretion rates. In addition, mass accretion rates of an additional 85 HAeBes are determined. We confirm previous findings that the mass accretion rate increases as a function of stellar mass, and the existence of a different slope for lower and higher mass stars, respectively. The mass where the slope changes is determined to be $3.98^{+1.37}_{-0.94} M_{\odot}$. We discuss this break in the context of different modes of disc accretion for low- and high-mass stars. Because of their similarities with T Tauri stars, we identify the accretion mechanism for the late-type Herbig stars with the Magnetospheric Accretion. The possibilities for the earlier-type stars are still open, we suggest the Boundary Layer accretion model may be a viable alternative. Finally, we investigated the mass accretion–age relationship. Even using the superior *Gaia* based data, it proved hard to select a large enough sub-sample to remove the mass dependence in this relationship. Yet, it would appear that the mass accretion does decline with age as expected from basic theoretical considerations.

Key words: accretion, accretion discs – techniques: spectroscopic – stars: formation – stars: fundamental parameters – stars: pre-main-sequence – stars: variables: T Tauri, Herbig Ae/Be.

1 INTRODUCTION

Herbig Ae/Be stars (HAeBes) are optically visible intermediate pre-main sequence (PMS) stars whose masses range from about 2 to $10 M_{\odot}$. These PMS stars were first identified by Herbig (1960), using three criteria: ‘Stars with spectral type A and B with emission lines; lie in an obscured region; and illuminate fairly bright nebulosity in its immediate vicinity’. HAeBes play an important role in understanding massive star formation, because they bridge the gap between low-mass stars whose formation is relatively well understood, and high-mass stars whose formation is still unclear. The study of their formation is not well understood as massive stars are very rare and as a consequence on average far away, and often optically invisible (Lumsden et al. 2013). A long standing problem has also been that their brightness is very high, such that

radiation pressure can, in principle, stop accretion on to the stellar surface (Kahn 1974). Moreover, they form very quickly and reach the main sequence before their surrounding cloud disperses (Palla & Stahler 1993). This suggests that their evolutionary processes are very different from T Tauri stars.

The accretion on to classical T Tauri low-mass stars is magnetically controlled. The magnetic field from the star truncates material in the disc and from this point, material falls on to the star along the field line. After matter hits the photosphere, it produces X-ray radiation that is absorbed by surrounding particles. Then, these particles heat up and re-radiate at ultraviolet (UV) wavelengths, producing an UV-excess that can be observed and from which the accretion luminosity can be calculated (Bouvier et al. 2007; Hartmann, Herczeg & Calvet 2016). It was found later, that a correlation between the line luminosity and the accretion luminosity exists, allowing accretion rates of classical T Tauri stars to be determined from the UV-excess and absorption line veiling (Calvet et al. 2004; Ingleby et al. 2013).

* E-mail: pycw@leeds.ac.uk (CW); r.d.oudmaijer@leeds.ac.uk (RDO)

HAeBes have similar properties as classical T Tauri stars, for instance having emission lines, UV-excess, a lower surface gravity than main-sequence stars (Hamann & Persson 1992; Vink et al. 2005) and they are usually identified by an infrared (IR) excess from circumstellar discs (Van den Ancker et al. 2000; Meeus et al. 2001). Because their envelopes are radiative, no magnetic field is expected to be generated in HAeBe stars as this usually happens in stars by convection. Indeed, magnetic fields have rarely been detected towards them (Catala et al. 2007; Alecian et al. 2013). As a result magnetically controlled accretion is not necessarily expected to apply in the case of the most massive objects, requiring another accretion mechanism. However, how the material arrives at the stellar surface in the absence of magnetic fields is still unclear.

Several lines of evidence have indicated a difference between the lower mass Herbig Ae and higher mass Herbig Be stars. Spectropolarimetric studies suggest that Herbig Ae stars and T Tauri stars may form in the same process (Vink et al. 2005; Ababakr, Oudmaijer & Vink 2017). Accretion rates of HAeBes are determined from the measurement of UV-excess (Mendigutia et al. 2011b) who have found that the relationship between the line luminosity and the accretion luminosity is similar to the classical T Tauri stars. A spectroscopic variability study suggests that a Herbig Ae star is undergoing magnetospheric accretion in the same manner as classical T Tauri stars (Schöller et al. 2016) while Mendigutia et al. (2011a) find the Herbig Be stars to have different $H\alpha$ variability properties than the Herbig Ae stars. Therefore, magnetically influenced accretion in HAeBes would still be possible. A study employing X-shooter spectra for 91 HAeBes was carried out by Fairlamb et al. (2015, 2017, hereafter F15 and F17, respectively). They determined the stellar parameters in a homogenous fashion, derived mass accretion rates from the UV-excess and found the relationship between accretion luminosity and line luminosity for 32 emission lines in the range 0.4–2.4 μm . A total of 47 objects in their sample were taken from Thé, de Winter & Pérez (1994, table 1), which to this date contains the strongest (candidate) members of the group. The Fairlamb papers were published before the *Gaia* parallaxes became available, and the distances used may need revision as these can affect parameters such as the radius, luminosity, stellar mass and mass accretion rate.

A *Gaia* astrometric study of 252 HAeBes was carried out by Vioque et al. (2018) hereafter V18. They presented parallaxes for all known HAeBes from the *Gaia* Data Release 2 (*Gaia* DR2) Catalogue (*Gaia* Collaboration et al. 2016, 2018). Also, they collected effective temperatures, optical and IR photometry, visual extinctions, $H\alpha$ equivalent widths, emission line profiles, and binarities from the literature. They derived distances, luminosities, masses, ages, IR excesses, and photometric variabilities for most of their sample. This is the largest astrometric study of HAeBes to date. These *Gaia* DR2 parallaxes are useful for improving the stellar parameters of the previous studies.

The main aim of this paper is to determine stellar parameters and accretion rates of 30 Northern HAeBes using a homogeneous approach, extending the mostly Southern F15 sample. In parallel, the results of F15 will be updated using the distances determined from the *Gaia* DR2 parallaxes and a redetermined extinction towards the objects. As such, this becomes the largest homogeneous spectroscopic analysis of HAeBes to date. In addition, the accretion rates of HAeBes in the V18 study are determined for the 104 objects for which $H\alpha$ emission line equivalent widths are collected from the literature or determined from archival spectra.

The structure of this paper is as follows. Section 2 presents the spectroscopic data observation of all targets. Details of observations,

instrumental setups and reduction procedures are given in this section. Section 3 and 4 detail the determination of stellar parameters and mass accretion rates. Sections 5 and 6 focus on the analysis and a discussion, respectively. Section 7 provides a summary of the main conclusions of this paper.

2 OBSERVATIONS AND DATA REDUCTION

2.1 Intermediate dispersion spectrograph and sample selection

The data were collected in June 2013 using the Intermediate dispersion spectrograph (IDS) instrument and the RED + 2 CCD detector with 2048×4096 pixels (pixel size $24 \mu\text{m}$), which is attached to the Cassegrain focus of the 2.54-m Isaac Newton Telescope (INT) at the Observatorio del Roque de los Muchachos, La Palma, Spain. The observations spanned six nights between 2013 June 20 and 25. Bias frames, flat-field frames, object frames, and arc frames of Cu-Ar and Cu-Ne comparison lamp were taken each night to prepare for the data reduction.

In the first two nights, the spectrograph was set up with a 1200 lines mm^{-1} R1200B diffraction grating and a 0.9 or 1.0 arcsec wide slit in order to obtain spectra across the Balmer discontinuity. The wavelength coverage was 3600–4600 \AA , centred at 4000.5 \AA . In this range, the hydrogen lines of $H\gamma$, $H\delta$, $H(7-2)$, $H(8-2)$, $H(9-2)$, and $H(10-2)$ can be analysed. This combination provides a reciprocal dispersion of $0.53 \text{\AA pixel}^{-1}$ with a spectral resolution of $\sim 1 \text{\AA}$ and a resolving power of $R \sim 4000$.

For the next two nights the R1200Y grating was used to observe spectra in the visible. Its spectral range covers 5700 to 6700 \AA , centred at 6050.4 \AA . This range includes the He I line at 5876 \AA , the $[\text{O I}_{\lambda 6300}]$ line and the $H\alpha$ line at 6562 \AA . This setup results in a reciprocal dispersion of $0.52 \text{\AA pixel}^{-1}$ and a resolving power of $R \sim 6500$. The final 2 nights used the R1200R grating to observe the spectral range of 8200–9200 \AA , centred at 8597.2 and 8594.4 \AA . This range covers the O I line at 8446 \AA , all lines of the Ca II triplet and many lines of the Paschen series. With this setup the reciprocal dispersion becomes $0.51 \text{\AA pixel}^{-1}$, giving a resolving power of $R \sim 9000$.

The sample consists of 45 targets, with 30 HAeBes, and 15 standard stars. A total of 26 Herbig stars were chosen from the catalogue of Thé et al. (1994, table 1) and 4 from Vieira et al. (2003). About 67 per cent of HAeBes in the final sample are in the Northern hemisphere. There are seven HAeBes that are also in the sample of F15. Spectra of standard stars were observed each night for spectral comparisons. A log of the observations of the 30 HAeBes is shown in Table 1 while a log of the observations of the standard stars is presented in Table A1 (See Appendix A in the online version of this paper).

The data reduction was performed using the Image Reduction and Analysis Facility (IRAF¹). Standard procedures were used in order to process all frames. Generally, there are three steps of data reduction; bias subtraction, flat-field division, and wavelength calibration. First, many bias frames were taken and averaged to reduce some noise and the bias level was removed from the CCD data. Next, flat-field division was used to remove the variations of

¹IRAF is distributed by the National Optical Astronomy Observatory, which is operated by the Association of Universities for Research in Astronomy (AURA) under a cooperative agreement with the National Science Foundation.

Table 1. Log of observations of 30 HAEs. Column 1 gives the object name. Columns 2 and 3 are right ascension (RA) in the units of time ($^{\text{h}}\text{m}^{\text{s}}$) and declination (Dec.) in the units of angle ($^{\circ}$ '), respectively. Column 4 lists the observation dates. Columns 5–7 present the exposure times for each grating. The signal-to-noise ratios for each grating are given in columns 8–10. These were determined using a 20 Å wide line free spectral regions centred at the wavelength 4200, 6050, and 8800 Å for R1200B, R1200Y, and R1200R gratings, respectively. Spectral types and photometry are listed along with references in columns 11–16.

Name	RA (J2000)	Dec. (J2000)	Obs date (June 2013)	Exposure time (s)			SNR			Spectral type	Photometry (mag)			I_c	
				R1200B	R1200Y	R1200R	B	Y	R		V	R_c	R		
V594 Cas	00:43:18.3	+61:54:40.1	21; 23; 24	600	600	600	152	160	50	B8 ¹	11.08	10.51	10.08	–	9.55 ¹³
PDS 144	15:49:15.3	–26:00:54.8	22; 24	–	900	900	–	97	83	A5 V ²	13.28	12.79	12.49	–	12.16 ²
HD 141569	15:49:57.8	–03:55:16.3	20; 22; 24	60	60	60	302	385	194	A0 Ve ³	7.23	7.13	7.08	–	7.02 ²
HD 142666	15:56:40.0	–22:01:40.0	20; 22; 24	90; 180	90; 150	150	19	147	47	A8 Ve ³	9.17	8.67	8.35	–	8.01 ²
HD 145718	16:13:11.6	–22:29:06.7	21; 23; 25	90	180	180	30	160	74	A8 IV ²	9.62	9.10	8.79	–	8.45 ²
HD 150193	16:40:17.9	–23:53:45.2	21; 23; 24; 25	90	300	120; 300	54	258	96	A2 IVe ³	9.33	8.80	8.41	–	7.93 ¹⁴
PDS 469	17:50:58.1	–14:16:11.8	23; 25	–	1200	1200	–	127	62	A0 ²	13.33	12.77	12.39	–	11.95 ²
HD 163296	17:56:21.3	–21:57:21.9	20; 23; 24; 25	60	60	60	60	270	125	A1 Vep ³	6.94	6.83	6.77	–	6.73 ¹⁴
MWC 297	18:27:39.5	–03:49:52.1	21; 22; 24; 25	900	10; 60	1200; 600	22	16	102	B0 ²	14.28	12.03	10.19	–	8.80 ¹⁴
VV Ser	18:28:47.9	+00:08:39.8	21; 23; 25	900	600	600	91	180	113	B6 ⁴	12.82	11.81	11.10	–	10.31 ¹³
MWC 300	18:29:25.7	–06:04:37.3	21; 23; 25	900	600; 60	600	48	29	19	B1 Ia + [e] ⁵	12.81	11.78	11.09	–	10.58 ¹⁴
AS 310	18:33:21.3	+04:58:04.8	20; 22; 24	40; 900	1200	1200	35	144	128	B1e ⁴	13.56	12.59	11.93	–	11.20 ¹⁴
PDS 543	18:48:00.7	+02:54:17.1	21; 22; 24	900	1200	1200	39	153	149	B1 ²	14.56	12.52	11.25	–	9.96 ²
HD 179218	19:11:11.3	+15:47:15.6	21; 23; 25	60	120	120	140	311	166	A0 IVe ³	7.47	7.39	7.34	–	7.29 ²
HD 190073	20:03:02.5	+05:44:16.7	21; 23; 25	60	120	120; 300	65	205	90	A0 IVp + sh ²	7.86	7.73	–	7.66 ¹⁵	–
V1685 Cyg	20:20:28.2	+41:21:51.6	20; 22; 24; 25	600	600; 60	600; 60	120	114	82	B2 Ve ³	11.48	10.69	–	9.63 ¹⁶	–
LkHA 134	20:48:04.8	+43:47:25.8	20; 22; 24	600	600	600	79	192	95	B8 ⁶	12.02	11.35	–	10.56 ¹⁶	–
HD 200775	21:01:36.9	+68:09:47.8	20; 22; 24; 25	60	60; 30	30; 60	161	192	50	B3 ⁴	7.77	7.37	–	6.84 ¹⁶	–
LkHA 324	21:03:54.2	+50:15:10.0	21; 23; 25	900	1200	1200	52	166	123	B8 ⁴	13.71	12.56	11.85	–	11.09 ¹³
HD 203024	21:16:03.0	+68:54:52.1	21; 23; 24; 25	120	180	180	56	187	65	A5 V ³	9.24	9.01	9.02	–	8.62 ¹⁷
V645 Cyg	21:39:58.3	+50:14:20.9	21; 23; 25	900	1200	1200	20	86	152	O8.5 ⁷	14.55	13.47	–	12.28 ¹⁶	–
V361 Cep	21:42:50.2	+66:06:35.1	20; 22; 24; 25	300	300	300	146	219	84	B4 ⁴	10.65	10.21	9.89	–	9.50 ¹³
V373 Cep	21:43:06.8	+66:06:54.2	20; 22; 24	900	1200	1200	96	143	103	B8 ⁸	13.22	12.33	11.7	–	11.01 ¹³
V1578 Cyg	21:52:34.1	+47:13:43.6	21; 23; 24; 25	900	300; 600	300	86	225	191	A0 ⁴	10.53	10.13	–	9.67 ¹⁶	–
LkHA 257	21:54:18.8	+47:12:09.7	20; 22; 23; 24	900	1200	1200	54	179	129	A2e ⁹	14.00	13.29	12.86	–	12.39 ¹⁷
SV Cep	22:21:33.2	+73:40:27.1	20; 22; 24	240	300	300	87	188	112	A2 IVe ³	11.37	10.98	–	10.58 ¹⁶	–
V375 Lac	22:34:41.0	+40:40:04.5	23; 25	–	1200	1200	–	109	71	A7 Ve ¹⁰	14.22	13.38	12.84	–	12.25 ¹³
HD 216629	22:53:15.6	+62:08:45.0	20; 22; 24	90	180	180	91	251	110	B3 IVe + A3 ¹¹	10.01	9.28	–	8.53 ¹⁶	–
V374 Cep	23:05:07.5	+62:15:36.5	20; 22; 24	600	450	450	121	173	138	B5 Vep ¹²	11.14	10.28	9.71	–	9.12 ¹⁷
V628 Cas	23:17:25.6	+60:50:43.4	21; 23; 24; 25	900	600; 60	600	26	130	149	B0eq ¹	12.63	11.37	10.38	–	9.37 ¹³

Notes. References. ⁽¹⁾Hillenbrand et al. (1992); ⁽²⁾Vieira et al. (2003); ⁽³⁾Mora et al. (2001); ⁽⁴⁾Hernández et al. (2004); ⁽⁵⁾Wolf & Stahl (1985); ⁽⁶⁾Herbig (1958); ⁽⁷⁾Clarke et al. (2006); ⁽⁸⁾Dahm & Hillenbrand (2015); ⁽⁹⁾Walker (1959); ⁽¹⁰⁾Calvet & Cohen (1978); ⁽¹¹⁾Skiff (2014); ⁽¹²⁾Garrison (1970); ⁽¹³⁾Fernandez (1995); ⁽¹⁴⁾De Winter et al. (2001); ⁽¹⁵⁾Oudmaijer et al. (2001); ⁽¹⁶⁾Herbst & Shevchenko (1999); ⁽¹⁷⁾Zacharias et al. (2013).

CCD signal in each pixel. All flat frames were averaged before subtracting the bias. Then, all of the object frames were divided by the normalised flat-field frame in order to correct the pixel-to-pixel variation of the detector sensitivity. The object frame was extracted to a one-dimensional spectrum by defining the extraction aperture on the centre of the profile and subtracting the sky background. Finally, the data were wavelength calibrated. The accuracy of the wavelength calibration is measured from an rms of the fit and is less than 10 per cent of the reciprocal dispersion ($<0.05 \text{ \AA pixel}^{-1}$). For illustration, the $H\alpha$ profiles of all 30 objects are displayed in Fig. B1 (See Appendix B in the online version of this paper).

3 STELLAR PARAMETERS AND MASS ACCRETION RATE DETERMINATIONS

Measurement of accretion rates requires accurate stellar parameters of the star in question. Therefore, this section aims to determine accretion rates by first determining the stellar parameters, such as the effective temperature, surface gravity, distance, radius, reddening, luminosity, mass, and age. These will be determined by combining the IDS spectra, stellar model atmosphere grids, photometry from the literature, the *Gaia* DR2 parallaxes, and stellar isochrones.

3.1 Effective temperature and surface gravity

To estimate the effective temperature of the target, a comparison of the known standard star spectra with the unknown target spectrum is performed. The list of standard stars including spectral types is shown in Table A1 (See Appendix A in the online version of this paper). The conversion from the spectral type to effective temperature can be found from Straižys & Kuriliene (1981). Then, the range of effective temperatures was explored in more detail with spectra computed from model atmospheres.

The model atmospheres used in this work are grids of BOSZ–Kurucz model atmospheres computed by Bohlin et al. (2017). The BOSZ models are calculated from ATLAS-APOGEE ATLAS9 (Mészáros et al. 2012) which came from the original ATLAS code version 9 (Kurucz 1993). The metallicity $[M/H] = 0$, carbon abundance $[C/H] = 0$, alpha-element abundance $[\alpha/H] = 0$, microturbulent velocity $\xi = 2.0 \text{ km s}^{-1}$, rotational broadening velocity $v \sin i = 0.0 \text{ km s}^{-1}$, and instrumental broadening $R = 5000$ are adopted. This instrumental broadening is chosen for matching the resolution of the blue spectra. The range of effective temperature T_{eff} is from 3500 to 30 000 K with steps of 250 K (from 3500 to 12 000 K), 500 K (from 12 000 to 20 000 K), and 1000 K (from 20 000 to 30 000 K). The range of surface gravity $\log(g)$ is from 0.0 to 5.0 dex with steps of 0.5 dex. By using linear interpolation, $\log(g)$ with steps of 0.1 dex were calculated.

The procedure to obtain the effective temperature and surface gravity in this work follows the same method by F15. The effective temperature and surface gravity determination is carried out by primarily comparing the wings of the observed hydrogen Balmer lines $H\gamma$, $H\delta$, and $H\epsilon$ with synthetic profiles produced with solar metallicity from BOSZ models. The shapes of the hydrogen profiles are not very sensitive to metallicity (Bohlin et al. 2017), while their widths are dominated by pressure broadening, while rotation hardly affects the shapes. $H\alpha$ is not used for spectral typing because it is frequently strongly in emission for HAeBes. This phenomenon can affect the shape of the wings and cause difficulty of fitting the BOSZ models to target spectra. $H\beta$ is also not used for spectral typing because it appears around the edge of the blue spectrum which makes a proper characterization of $H\beta$'s line profile troublesome.

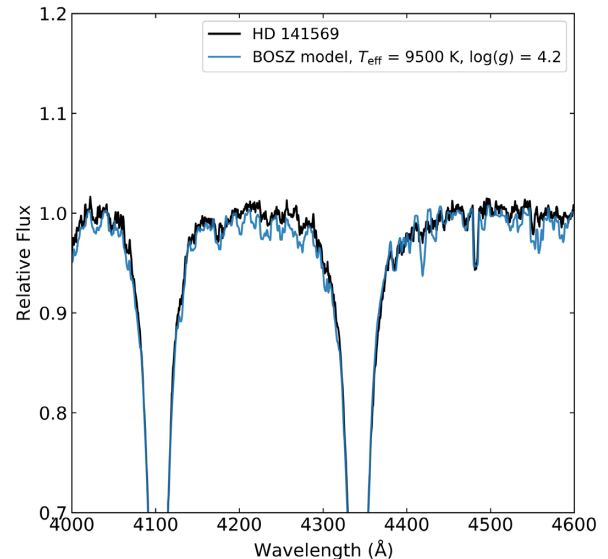


Figure 1. The normalised spectrum of HD 141569 fits with BOSZ model of $T_{\text{eff}} = 9500 \text{ K}$ and $\log(g) = 4.2$.

In order to carry out the fitting, both the observed profiles and the synthetic profiles are normalised based on the continuum on both the blue and red side of the profile. Next, the observed wavelengths of the target profiles were corrected to the vacuum wavelength of the synthetic profile using the IRAF DOPCOR task. The effective temperature and surface gravity are obtained from the fit of the normalised synthetic spectra to the normalised observed spectra by considering continuum features and the wings of the profile above the normalised intensity of 0.8. This intensity was chosen because this part of the wings is sensitive to variation of the $\log(g)$ while the central part of the profile of a Herbig Ae/Be star can be contaminated by emission.

The width of the Balmer lines depends upon both effective temperature and surface gravity. Different combinations of T_{eff} and $\log(g)$, can create the same width. This degeneracy can be solved by visual inspection of absorption features in the wings and continuum either side of the lines. The final value for the effective temperature and surface gravity are the average value of the best fit for each profile ($H\gamma$, $H\delta$, and $H\epsilon$). The uncertainties of T_{eff} and $\log(g)$ were chosen to be the typical difference in the values determined for the three lines, respectively. If the standard error becomes zero or less than that, the step size will be adopted. An example of spectral typing by fitting the Balmer line profile of HD 141569 (black) and the BOSZ model (blue) is demonstrated in Fig. 1.

For a given T_{eff} , normally, the higher the $\log(g)$, the broader the Balmer profile. Therefore, the region of the wings of the hydrogen profile near the continuum level can be used to obtain both effective temperature and surface gravity as mentioned earlier. Unfortunately, there is a non-linear relationship between the surface gravity and width of the Balmer profile for objects that have $T_{\text{eff}} < 8000 \text{ K}$. For this reason, a spectroscopic $\log(g)$ cannot be determined and the surface gravity is calculated instead using the stellar mass and radius (see later). For three objects (PDS 144S, PDS 469, and V375 Lac) no near UV blue spectra were taken during the observations. Fortunately, a FEROS spectrum of PDS 469² was found in the ESO

²Based on observations collected at the European Southern Observatory under ESO programmes 084.A-9016(A).

Science Archive Facility and was used to determine temperature and surface gravity. In the case of PDS 144S and V375 Lac, visible spectra including H α profiles in combination with spectral types from the literature were investigated in order to adopt their effective temperatures.

Seven objects show extremely strong emission lines. These strong emissions have an influence on the wings on even the whole Balmer profiles. Both T_{eff} and $\log(g)$ could therefore not be determined by this method. Instead, for these objects, estimated temperatures from the literature are adopted. The stars for which this process is performed on are noted in the last column of Table 2.

There are 7 objects in this work that overlap with F15. The difference in temperatures of these objects is on average 180 K, which is smaller than the step-size used by both studies. Fig. 2 compares the effective temperature derived in this work (Table 2) with estimated values from the literature. The good correlation would suggest that our method is reliable, the fact that it is applied to the entire sample ensures a homogeneous study.

3.2 Visual extinction, distance, and radius

The second step is to use the synthetic BOSZ spectral energy distribution and previous photometry results to determine the visual extinction or reddening (A_V) by fitting the synthetic surface flux density to observed photometry. In the case of zero extinction or for extinction corrected photometry, the flux density f of the BOSZ model and the observed fluxes differ by the ratio of distance to the star and its radius (D/R_*). The spectral energy distribution grid of the BOSZ models are set up for the effective temperatures from the previous step with a range of scaling factors D/R_* . The value of $\log(g)$ does not have a significant effect on the spectral energy distribution shape. Therefore, $\log(g) = 4.0$ was adopted at this stage.

The observed photometry is dereddened using the extinction values A_V/A_V from Cardelli, Clayton & Mathis (1989) with the standard ratio of total to selective extinction parameter $R_V = 3.1$ and zero-magnitude fluxes from Bessell (1979). By varying A_V in steps of 0.01 magnitude, the best fit of the photometry and BOSZ models will then yield the best-fitting reddening values. Only the BVR_I magnitudes are used, as the U -band and $JHKLM$ photometry are often affected by the Balmer continuum excess and IR-excess emission, respectively, i.e. they cannot automatically be used in the fitting. All of the observed BVR_cI_c or BVR photometry from the literature are shown in Table 1. For three objects (HD 203024, LkHA 257, and V374 Cep) their Sloan photometry needed to be converted to Johnson–Cousins photometry. This was done using the transformation equations provided by Smith et al. (2002). The uncertainties in the resulting A_V and D/R_* are assigned to be at values that resulted twice of the minimum chi-squared value. Fig. 3 demonstrates an example of photometry fitting.

The scaling factor D/R_* allows us to calculate stellar radius R_* , provided the stellar distance D is known. The *Gaia* DR2 catalogue provides astrometric parameters, such as positions, proper motions and parallaxes for more than 1.3 billion targets including most of the known HAeBes. The distances to most of our targets were determined by V18 using *Gaia* DR2 parallaxes. Re-normalised unit weight error (RUWE) is used to select sources with good astrometry. We adopted $\text{RUWE} < 1.4$ as a criterion for good parallaxes (see *Gaia* Data Release 2 document). Seven stars have low quality parallaxes, and for two stars no parallaxes are presented in the *Gaia* archive. These are noted in the final column of Table 2. In total, stellar radii could be determined for 26 out of the 30 targets.

3.3 Stellar luminosity, mass, and age

Using the stellar radius R_* and the effective temperature T_{eff} , the luminosity L_* can be determined from the Stefan–Boltzmann law. The next step is to estimate the mass and age of the HAeBes using isochrones. Stellar isochrones of Marigo et al. (2017) from 0.01 to 100 Myr are used in order to extract a mass and an age of the target from the luminosity–temperature Hertzsprung–Russell (HR) diagram. A metallicity $Z = 0.01$ and helium mass fraction $Y = 0.267$ are chosen, because these values are close to solar values.

After each star is placed on the HR diagram, the two closest points on an isochrone are used to obtain the mass of the star by interpolating between those points. Uncertainties of mass and age are derived from the error bars of the effective temperature T_{eff} and the luminosity L_* on the HR diagram. All determined parameters of all targets are presented in Table 2. The positions of the 21 HAeBes on the HR diagram are represented with red symbols in Fig. 4. As mentioned above, the 9 targets that are not included in the plot have low quality parallaxes or do not have parallaxes at all. Since the three objects (HD 142666, HD 145718, and SV Cep) have had $T_{\text{eff}} < 8000$ K, their surface gravity cannot be determined from fitting the spectra with stellar atmospheric models. Instead, their surface gravities were calculated from the stellar mass and radius derived from the parallaxes instead. These are also noted in the $\log(g)$ column of Table 2.

3.4 Extending the sample with HAeBes in the Southern hemisphere

The original driver for the INT observations presented here was to extend the spectroscopic analysis of the, mostly southern, sample of F15 to the Northern hemisphere. However, F15 determined spectroscopic distances using their spectral derived values of the surface gravity or literature values for the distances to their 91 HAeBes. The availability of *Gaia*-derived distances warrants a re-determination of the stellar parameters. To this end, we use the distances from the *Gaia* DR2 parallax (V18). In parallel, we re-assessed the extinction values using the same photometric bands BVR_cI_c as above to ensure consistency in the determination of the extinction. Most of the photometry used for the photometry fitting can be found in F15 (table A1). We collated Sloan photometry from Zacharias et al. (2013) for three objects (HD 290500, HT CMA, and HD 142527) and one object, HD 95881, from APASS³ DR10 and converted these to the Johnson–Cousins system. Moreover, we also used the brightest V -band magnitude of Johnson BVR photometry for 2 objects, HD 250550 and KK Oph, and Johnson BVR_I photometry for Z CMA from Herbst & Shevchenko (1999). The redetermined stellar parameters for the 91 HAeBes from F15 are listed in Table C1 (See Appendix C in the online version of this paper). For the sample as a whole, the luminosities resulting from the revised distances and extinctions are on average similar to the original F15 values, however the contribution to the scatter around the mean differences is dominated by the new distances. We thus conclude that the improvement in distance values dominates that of the extinction when arriving at the final luminosities.

We now have the largest spectroscopic sample of HAeBes and the homogeneously determined stellar parameters including mass accretion rates, which will be determined in the next section. Seven targets in F15's sample that are also in this work's sample were left

³AAVSO Photometric All-Sky Survey (APASS), funded by the Robert Martin Ayers Sciences Fund and NSF AST-1412587.

Table 2. Determined stellar parameters. Columns 2–9 are effective temperature, surface gravity, visual extinction, distance, radius, luminosity, mass, and age, respectively. Distance D in column 5 is obtained from Vioque et al. (2018).

Name	T_{eff} (K)	$\log(g)$ [cm s $^{-2}$]	A_V (mag)	D (pc)	R_* (R_{\odot})	$\log(L_*)$ [L_{\odot}]	M_* (M_{\odot})	Age (Myr)
V594 Cas	11500 $^{+250}_{-250}$	3.70 $^{+0.10}_{-0.10}$	2.27 $^{+0.18}_{-0.23}$	569 $^{+16}_{-14}$	3.86 $^{+0.52}_{-0.53}$	2.37 $^{+0.15}_{-0.17}$	3.51 $^{+0.45}_{-0.42}$	1.20 $^{+0.53}_{-0.38}$
PDS 144S	7750 $^{+500a}_{-500}$	4.00 $^{+0.30}_{-0.30}$	1.02 $^{+0.07}_{-0.07}$	d	–	–	–	–
HD 141569	9500 $^{+250}_{-250}$	4.20 $^{+0.10}_{-0.10}$	0.38 $^{+0.02}_{-0.03}$	110.63 $^{+0.91}_{-0.88}$	1.74 $^{+0.03}_{-0.04}$	1.34 $^{+0.06}_{-0.07}$	2.06 $^{+0.02}_{-0.15}$	5.80 $^{+1.87}_{-0.64}$
HD 142666	7250 $^{+250}_{-250}$	4.00 $^{+0.10c}_{-0.10}$	0.82 $^{+0.07}_{-0.08}$	148.3 $^{+2}_{-1.9}$	2.21 $^{+0.11}_{-0.12}$	1.08 $^{+0.10}_{-0.11}$	1.64 $^{+0.12}_{-0.11}$	7.76 $^{+1.79}_{-1.30}$
HD 145718	7750 $^{+250}_{-250}$	4.20 $^{+0.10c}_{-0.10}$	1.10 $^{+0.06}_{-0.06}$	152.5 $^{+3.2}_{-3}$	1.85 $^{+0.10}_{-0.10}$	1.05 $^{+0.10}_{-0.10}$	1.62 $^{+0.07}_{-0.03}$	8.71 $^{+0.84}_{-1.12}$
HD 150193	9250 $^{+250}_{-250}$	4.10 $^{+0.10}_{-0.10}$	1.88 $^{+0.16}_{-0.20}$	150.8 $^{+2.7}_{-2.5}$	2.34 $^{+0.26}_{-0.27}$	1.56 $^{+0.14}_{-0.15}$	2.12 $^{+0.21}_{-0.12}$	4.57 $^{+0.93}_{-1.02}$
PDS 469	9500 $^{+750a}_{-750}$	3.80 $^{+0.30}_{-0.30}$	1.94 $^{+0.12}_{-0.13}$	d	–	–	–	–
HD 163296	9000 $^{+250}_{-250}$	4.10 $^{+0.10}_{-0.10}$	0.20 $^{+0.01}_{-0.02}$	101.5 $^{+2}_{-1.9}$	1.87 $^{+0.05}_{-0.05}$	1.31 $^{+0.07}_{-0.07}$	1.95 $^{+0.07}_{-0.07}$	6.03 $^{+0.28}_{-0.27}$
MWC 297	24000 $^{+2000bb}_{-2000}$	4.00 $^{+0.10}_{-0.10}$	7.87 $^{+0.41}_{-0.64}$	375 $^{+22}_{-18}$	9.28 $^{+3.12}_{-3.04}$	4.41 $^{+0.39}_{-0.50}$	14.53 $^{+6.11}_{-4.84}$	0.04 $^{+0.07}_{-0.02}$
VV Ser	14000 $^{+1000}_{-1000}$	4.30 $^{+0.30}_{-0.30}$	3.74 $^{+0.22}_{-0.27}$	d	–	–	–	–
MWC 300	23000 $^{+2000b}_{-2000}$	3.00 $^{+0.20}_{-0.20}$	3.85 $^{+0.21}_{-0.28}$	1400 $^{+250}_{-160}$	6.02 $^{+1.96}_{-1.44}$	3.96 $^{+0.39}_{-0.39}$	10.09 $^{+3.76}_{-1.89}$	0.09 $^{+0.09}_{-0.05}$
AS 310	26000 $^{+2000}_{-2000}$	4.40 $^{+0.35}_{-0.35}$	3.86 $^{+0.20}_{-0.24}$	2110 $^{+350}_{-240}$	5.70 $^{+1.71}_{-1.27}$	4.13 $^{+0.36}_{-0.36}$	11.60 $^{+3.92}_{-2.18}$	0.07 $^{+0.08}_{-0.04}$
PDS 543	28500 $^{+2500b}_{-2500}$	4.00 $^{+0.10}_{-0.10}$	7.11 $^{+0.28}_{-0.40}$	1410 $^{+240}_{-160}$	16.24 $^{+5.99}_{-4.57}$	5.19 $^{+0.42}_{-0.45}$	30.02 $^{+18.28}_{-10.85}$	0.01 $^{+0.01}_{-0.01}$
HD 179218	9500 $^{+250}_{-250}$	3.95 $^{+0.10}_{-0.10}$	0.33 $^{+0.02}_{-0.02}$	266 $^{+5.6}_{-5.2}$	3.62 $^{+0.12}_{-0.11}$	1.98 $^{+0.07}_{-0.07}$	2.86 $^{+0.16}_{-0.20}$	2.04 $^{+0.47}_{-0.26}$
HD 190073	9750 $^{+250}_{-250}$	3.50 $^{+0.10}_{-0.10}$	0.20 $^{+0.04}_{-0.04}$	870 $^{+100}_{-70}$	9.23 $^{+1.28}_{-0.94}$	2.84 $^{+0.16}_{-0.14}$	5.62 $^{+0.78}_{-0.65}$	0.28 $^{+0.14}_{-0.10}$
V1685 Cyg	23000 $^{+4000b}_{-4000}$	4.06 $^{+0.10}_{-0.10}$	3.33 $^{+0.34}_{-0.51}$	910 $^{+46}_{-39}$	5.48 $^{+1.51}_{-1.51}$	3.88 $^{+0.49}_{-0.61}$	9.53 $^{+4.57}_{-2.55}$	0.11 $^{+0.27}_{-0.07}$
LkHA 134	11000 $^{+250}_{-250}$	4.00 $^{+0.10}_{-0.10}$	2.44 $^{+0.19}_{-0.24}$	843 $^{+36}_{-31}$	4.53 $^{+0.71}_{-0.70}$	2.43 $^{+0.17}_{-0.19}$	3.77 $^{+0.56}_{-0.56}$	1.02 $^{+0.60}_{-0.34}$
HD 200775	19000 $^{+3000}_{-3000}$	4.27 $^{+0.25}_{-0.25}$	1.85 $^{+0.15}_{-0.17}$	d	–	–	–	–
LkHA 324	12500 $^{+500}_{-500}$	4.00 $^{+0.10}_{-0.10}$	3.94 $^{+0.14}_{-0.16}$	605 $^{+16}_{-14}$	3.15 $^{+0.34}_{-0.33}$	2.34 $^{+0.16}_{-0.17}$	3.36 $^{+0.41}_{-0.30}$	1.51 $^{+0.49}_{-0.41}$
HD 203024	8500 $^{+500}_{-500}$	3.83 $^{+0.29}_{-0.29}$	0.52 $^{+0.24}_{-0.31}$	e	–	–	–	–
V645 Cyg	30000 $^{+7000b}_{-7000}$	3.75 $^{+0.35}_{-0.35}$	4.21 $^{+0.29}_{-0.40}$	d	–	–	–	–
V361 Cep	16750 $^{+500}_{-500}$	4.00 $^{+0.10}_{-0.10}$	1.97 $^{+0.14}_{-0.15}$	893 $^{+35}_{-31}$	4.34 $^{+0.52}_{-0.48}$	3.12 $^{+0.15}_{-0.15}$	5.56 $^{+0.65}_{-0.57}$	0.40 $^{+0.16}_{-0.11}$
V373 Cep	11500 $^{+1250b}_{-1250}$	3.50 $^{+0.50}_{-0.50}$	3.24 $^{+0.20}_{-0.23}$	d	–	–	–	–
V1578 Cyg	10500 $^{+500}_{-500}$	3.80 $^{+0.20}_{-0.20}$	1.46 $^{+0.08}_{-0.08}$	773 $^{+30}_{-27}$	4.77 $^{+0.41}_{-0.37}$	2.39 $^{+0.15}_{-0.15}$	3.74 $^{+0.45}_{-0.41}$	1.02 $^{+0.39}_{-0.28}$
LkHA 257	9250 $^{+250}_{-250}$	4.05 $^{+0.10}_{-0.10}$	2.28 $^{+0.07}_{-0.08}$	794 $^{+18}_{-16}$	1.84 $^{+0.11}_{-0.11}$	1.35 $^{+0.10}_{-0.10}$	1.98 $^{+0.06}_{-0.04}$	5.76 $^{+1.32}_{-0.51}$
SV Cep	8000 $^{+500}_{-500}$	4.37 $^{+0.11c}_{-0.11}$	0.78 $^{+0.04}_{-0.05}$	344.3 $^{+4}_{-3.8}$	1.48 $^{+0.05}_{-0.06}$	0.91 $^{+0.14}_{-0.15}$	1.63 $^{+0.04}_{-0.14}$	11.00 $^{+10.40}_{-2.49}$
V375 Lac	8000 $^{+750a}_{-750}$	4.30 $^{+0.10}_{-0.10}$	2.31 $^{+0.14}_{-0.16}$	e	–	–	–	–
HD 216629	21500 $^{+1000}_{-1000}$	4.00 $^{+0.10}_{-0.10}$	2.80 $^{+0.13}_{-0.15}$	805 $^{+31}_{-27}$	7.59 $^{+0.94}_{-0.83}$	4.04 $^{+0.18}_{-0.18}$	10.83 $^{+1.71}_{-1.54}$	0.07 $^{+0.04}_{-0.02}$
V374 Cep	15500 $^{+1000}_{-1000}$	3.50 $^{+0.10}_{-0.10}$	3.20 $^{+0.15}_{-0.18}$	872 $^{+40}_{-35}$	7.72 $^{+1.05}_{-0.98}$	3.49 $^{+0.22}_{-0.23}$	7.50 $^{+1.46}_{-1.28}$	0.16 $^{+0.12}_{-0.06}$
V628 Cas	31000 $^{+5000b}_{-5000}$	4.00 $^{+0.10}_{-0.10}$	5.05 $^{+0.36}_{-0.55}$	d	–	–	–	–

^aStars for which near UV-B spectra were not obtained.

^bStars which display extremely strong emission lines.

^cStars for which parallactic $\log(g)$ is used.

^dStars which have low quality parallaxes in the *Gaia* DR2 Catalogue (see the text for discussion).

^eStars which do not have parallaxes in the *Gaia* DR2 Catalogue.

out, leaving 84 HAeBes in their sample. Unfortunately, 22 out of the 84 objects (not including PDS 144S) have low quality or do not have a *Gaia* DR2 parallax. These objects cannot be placed on the HR diagram at this stage. The final sample contains 83 Herbig Ae/Be objects. Fig. 4 demonstrates all these HAeBes (21 + 62) placed in the HR diagram. Many targets are gathered around 2 M_{\odot} and few targets are located at high-mass tracks. This can be understood by the initial mass function (Salpeter 1955). Low-mass stars are more common than high-mass stars. Moreover, low-mass stars evolve slower across the HR diagram.

3.5 Combining with additional HAeBes with *Gaia* DR2 data from V18

In order to expand the sample further, the rest of 144/252 objects in the sample of V18 were investigated. There are 101 objects

which satisfy the condition $\text{RUWE} < 1.4$. They are also included in Fig. 4. $\text{H}\alpha$ equivalent widths are provided for most objects in Vioque et al. (2018, their tables 1 and 2) with references. Spectra for 14 objects without $\text{H}\alpha$ data in the V18 sample were found in the ESO Science Archive Facility. These were downloaded and their $\text{H}\alpha$ equivalent widths (EWs) were measured. The stellar radii and surface gravities were calculated using the temperatures, luminosities, and masses provided in V18. The intrinsic equivalent widths were measured from BOSZ models for the temperature provided in Vioque et al. (2018, tables 1 and 2) and the calculated surface gravity. This will enable us to compute mass accretion rates for a further 85 objects below. Table D1 presents all of the emission lines measurements and determined accretion rates of the V18 sample (See Appendix D in the online version of this paper).

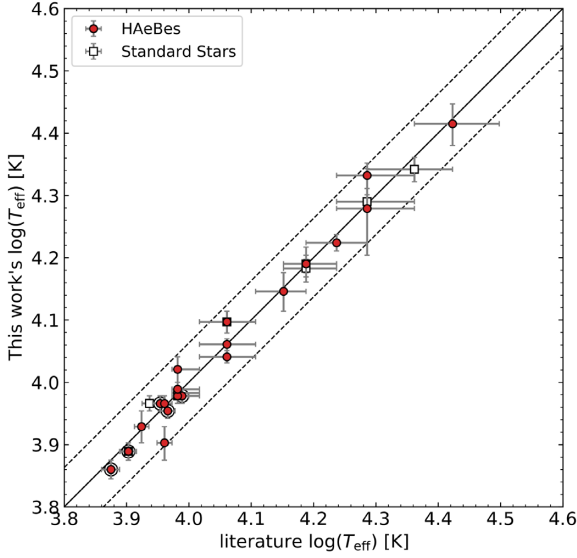


Figure 2. The effective temperature derived in this work compared to temperatures derived from spectral types in the literature listed in Tables 1 and A1. The spectral type was converted to temperature using the values provided in Straižys & Kuriliene (1981), and an uncertainty of a subclass of spectral type was assigned for the temperature. H AeBes and standard stars are denoted in circle and square, respectively. Circles with larger circle around them indicate the objects that temperature from F15 is used. The standard deviation (σ) between both $\log(T_{\text{eff}})$ is only 0.02. The solid line is the expected line of correlation and the dashed lines are 3σ deviation from the solid line.

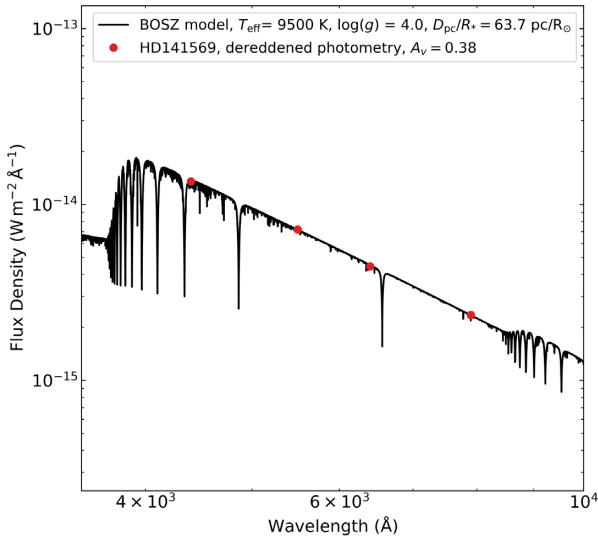


Figure 3. The synthetic spectral energy distribution BOSZ model (black line) is fitted to the dereddened photometry (red point) of HD 141569. The observed BVR_cI_c photometry of HD 141569 were taken from Vieira et al. (2003). A synthetic spectral energy distribution BOSZ model with $T_{\text{eff}} = 9500$ K and $\log(g) = 4.0$ is fitted to the dereddened photometry. This provides the reddening $A_V = 0.38^{+0.02}_{-0.03}$ mag and the scaling factor $D/R_* = 63.7^{+1.1}_{-0.7}$ pc/ R_{\odot} .

4 ACCRETION RATE DETERMINATION

We now will determine the mass accretion rates of the combined sample of H AeBes. The underlying assumption of the methodology is that the stars accrete material according to the MA paradigm, which, as demonstrated by Muzerolle et al. (2004), can explain the observed excess fluxes in H AeBes. The infalling material shocking the photosphere gives rise to UV-excess emission, whose measurement can be converted into an accretion luminosity. Knowledge of the stellar parameters can then return a value of the mass accretion rate.

F15 derived the accretion rates for their sample from the UV excess following the methodology of Muzerolle et al. (2004) and extending the work of Mendigutía et al. (2011b). Unfortunately, as mentioned before, our current observational set-up did not allow for such accurate measurements. However, as for example pointed out by Mendigutía et al. (2011b), the accretion luminosity correlates with the line strengths of various types of emission lines. They will therefore also correlate with the mass accretion rate (see also F17). As such, the line strengths do provide an observationally cheap manner to derive the accretion rate of an object without having to resort to the rather delicate and time-consuming process of measuring the UV excess. We should note that despite this, it is not clear whether the observed correlation is intrinsically due to accretion or some other effect (Mendigutía et al. 2015a).

We have chosen the $H\alpha$ line for the accretion luminosity determination, as these lines are strongest lines present in the spectra. To arrive at a measurement of the total line emission, we need to take account of the fact that the underlying line absorption is filled in with emission. Therefore, the intrinsic absorption equivalent width EW_{int} needs to be subtracted from the observed equivalent width EW_{obs} . The intrinsic EW is measured from the synthetic spectra corresponding to the effective temperature and surface gravity determined earlier.

The line luminosity L_{line} was calculated using the unreddened stellar flux at the wavelength of $H\alpha$ and distance to the star. The relationship between accretion luminosity and line luminosity goes as (cf. e.g. Mendigutía et al. 2011b).

$$\log\left(\frac{L_{\text{acc}}}{L_{\odot}}\right) = A + B \times \log\left(\frac{L_{\text{line}}}{L_{\odot}}\right), \quad (1)$$

where A and B are constants corresponding to the intercept and the gradient of the relation between $\log(L_{\text{acc}}/L_{\odot})$ and $\log(L_{\text{line}}/L_{\odot})$, respectively. This relationship has, most recently, been determined for 32 accretion diagnostic emission lines by F17. For the case of $H\alpha$, the constants are $A = 2.09 \pm 0.06$ and $B = 1.00 \pm 0.05$. The mass accretion rate is then determined from the accretion luminosity, stellar radius and stellar mass by equation (2).

$$\dot{M}_{\text{acc}} = \frac{L_{\text{acc}} R_*}{GM_*} \quad (2)$$

Table 3 summarises the EW measurements for the $H\alpha$ line and mass accretion rates in all H AeBes.

The final set of 78 mass accretion rates (21 + 57) based on the INT and X-Shooter data is the largest, and arguably the best such collection to date as they were determined in a homogeneous and consistent manner. To arrive at the largest sample possible however, we expand the sample using data provided in the comprehensive

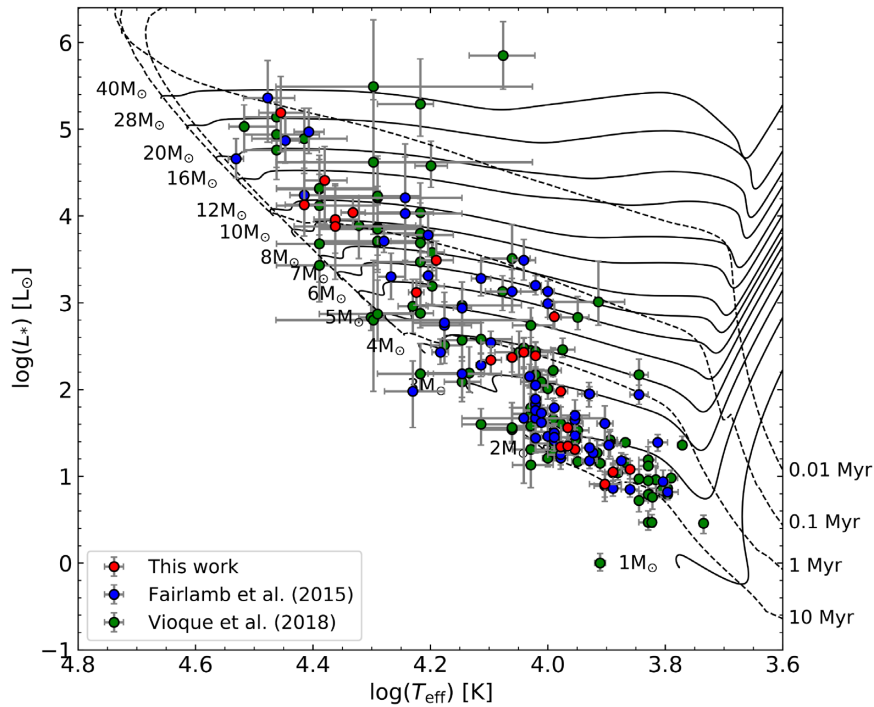


Figure 4. The placement of all 184 HAeBes in the HR diagram. The red circles are the work sample of 21 HAeBes, whereas 62 HAeBes in the sample of [F15](#) are denoted as the blue circles and 101 HAeBes in [Vioque et al. \(2018\)](#) are shown as the green circles. All of these objects satisfy the condition $\text{RUWE} < 1.4$. The PMS tracks with initial mass from 1 to $40 M_{\odot}$ ([Bressan et al. 2012](#); [Tang et al. 2014](#)) are plotted as solid lines and isochrones of 0.01, 0.1, 1, and 10 Myr ([Marigo et al. 2017](#)) are plotted as dashed lines.

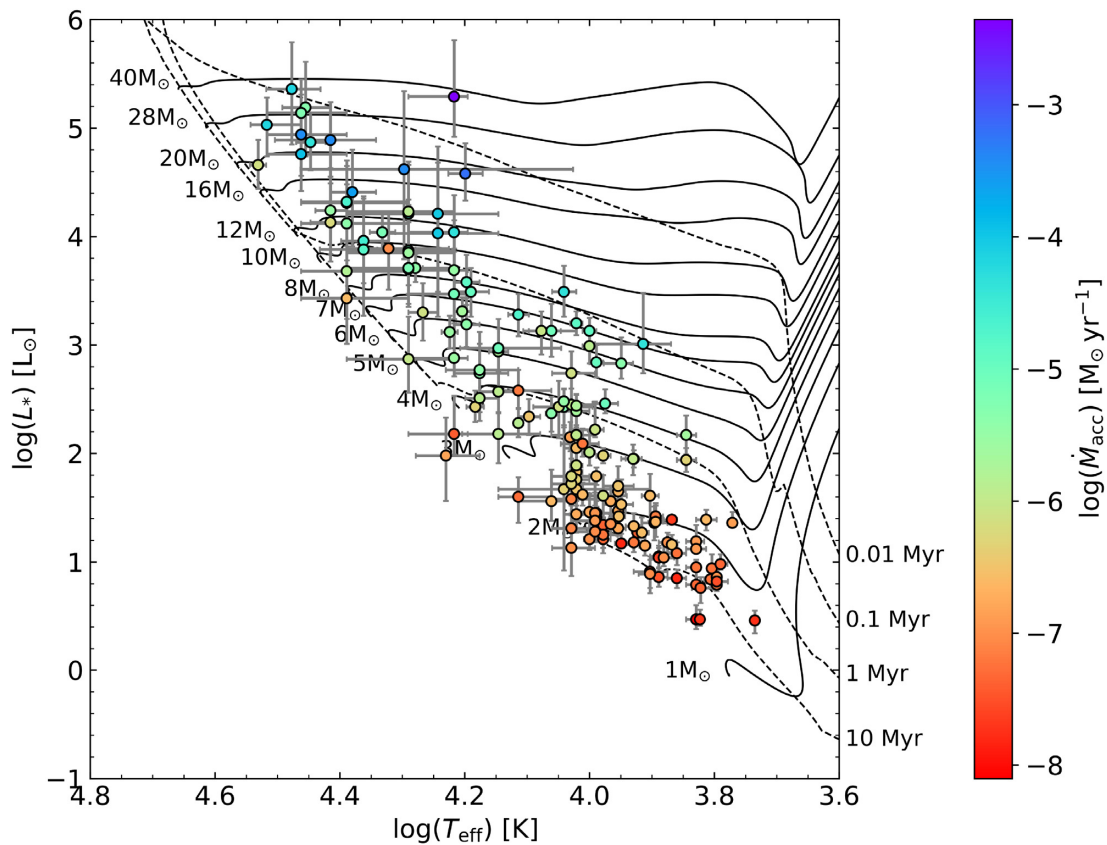


Figure 5. The placement of all 163 HAeBes in the HR diagram. The PMS tracks with initial mass from 1 to $40 M_{\odot}$ ([Bressan et al. 2012](#); [Tang et al. 2014](#)) and isochrones of 0.01, 0.1, 1, and 10 Myr ([Marigo et al. 2017](#)) are plotted as solid and dashed lines, respectively. The colour map denotes the accretion rate.

Table 3. The equivalent width measurements and accretion rates. Column 2 provides the H α emission line profile classification scheme according to Reipurth, Pedrosa & Lago (1996): single-peaked (I); double-peaked and the secondary peak rises above half strength of the primary peak (II); double-peaked and the secondary peak rises below half strength of the primary peak (III), when the secondary peak is located blueward or redward of the primary peak, class II and III are label with B or R, respectively; regular P-Cygni profile (IV B); and inverse P-Cygni profile (IV R). The classifications are based on the emission lines in Fig. B1 corrected for absorption. Columns 3–10 present observed equivalent width, intrinsic equivalent width, corrected equivalent width, continuum flux density at central wavelength of the H α profile, line flux, line luminosity, accretion luminosity, and mass accretion rate, respectively.

Name	H α profile	EW _{obs} (Å)	EW _{int} (Å)	EW _{cor} (Å)	F_{λ} ($\text{W m}^{-2} \text{Å}^{-1}$)	F_{line} (W m^{-2})	$\log(L_{\text{line}})$ [L_{\odot}]	$\log(L_{\text{acc}})$ [L_{\odot}]	$\log(\dot{M}_{\text{acc}})$ [$M_{\odot} \text{yr}^{-1}$]
V594 Cas	IV B	-81.79 ± 1.23	8.21 ± 0.19	-90.00 ± 1.24	1.11×10^{-15}	$(9.96 \pm 0.14) \times 10^{-14}$	$0.00^{+0.03}_{-0.03}$	$2.09^{+0.09}_{-0.09}$	$-5.36^{+0.09}_{-0.10}$
PDS 144S	I	-14.55 ± 0.53	12.82 ± 0.14	-27.37 ± 0.55	4.70×10^{-17}	$(1.29 \pm 0.03) \times 10^{-15}$	-	-	-
HD 141569	II R	6.38 ± 0.01	14.80 ± 0.26	-8.42 ± 0.26	4.17×10^{-15}	$(3.51 \pm 0.11) \times 10^{-14}$	$-1.87^{+0.02}_{-0.02}$	$0.22^{+0.17}_{-0.18}$	$-7.35^{+0.18}_{-0.15}$
HD 142666	IV R	2.46 ± 0.08	11.01 ± 0.17	-8.54 ± 0.19	1.84×10^{-15}	$(1.57 \pm 0.04) \times 10^{-14}$	$-1.97^{+0.02}_{-0.02}$	$0.12^{+0.18}_{-0.18}$	$-7.24^{+0.17}_{-0.17}$
HD 145718	I	10.83 ± 0.42	14.18 ± 0.25	-3.35 ± 0.49	1.50×10^{-15}	$(5.03 \pm 0.73) \times 10^{-15}$	$-2.44^{+0.08}_{-0.09}$	$-0.35^{+0.26}_{-0.27}$	$-7.79^{+0.26}_{-0.29}$
HD 150193	III B	-0.29 ± 0.05	14.86 ± 0.18	-15.15 ± 0.19	3.85×10^{-15}	$(5.83 \pm 0.07) \times 10^{-14}$	$-1.38^{+0.02}_{-0.02}$	$0.71^{+0.15}_{-0.15}$	$-6.75^{+0.15}_{-0.18}$
PDS 469	I	4.65 ± 0.17	13.50 ± 0.17	-8.85 ± 0.24	1.02×10^{-16}	$(9.04 \pm 0.24) \times 10^{-16}$	-	-	-
HD 163296	I	-11.04 ± 0.87	15.48 ± 0.13	-26.51 ± 0.88	5.11×10^{-15}	$(1.35 \pm 0.05) \times 10^{-13}$	$-1.36^{+0.03}_{-0.03}$	$0.73^{+0.16}_{-0.16}$	$-6.79^{+0.15}_{-0.16}$
MWC 297	I	-455.84 ± 1.41	3.50 ± 0.02	-459.34 ± 1.41	4.81×10^{-14}	$(2.21 \pm 0.01) \times 10^{-11}$	$1.99^{+0.05}_{-0.04}$	$4.08^{+0.21}_{-0.20}$	$-3.61^{+0.19}_{-0.20}$
VV Ser	II R	-39.07 ± 0.10	8.04 ± 0.07	-47.11 ± 0.12	1.31×10^{-15}	$(6.15 \pm 0.02) \times 10^{-14}$	-	-	-
MWC 300	III B	-140.04 ± 0.40	1.95 ± 0.06	-141.99 ± 0.40	1.35×10^{-15}	$(1.91 \pm 0.01) \times 10^{-13}$	$1.07^{+0.14}_{-0.21}$	$3.16^{+0.26}_{-0.21}$	$-4.56^{+0.24}_{-0.24}$
AS 310	I	0.83 ± 0.04	4.13 ± 0.03	-3.29 ± 0.05	6.60×10^{-16}	$(2.17 \pm 0.03) \times 10^{-15}$	$-0.52^{+0.11}_{-0.11}$	$1.57^{+0.22}_{-0.20}$	$-6.23^{+0.21}_{-0.22}$
PDS 543	I	0.16 ± 0.01	2.66 ± 0.02	-2.50 ± 0.02	1.42×10^{-14}	$(3.55 \pm 0.02) \times 10^{-14}$	$0.34^{+0.14}_{-0.11}$	$2.43^{+0.22}_{-0.18}$	$-5.33^{+0.15}_{-0.13}$
HD 179218	I	-1.70 ± 0.05	12.43 ± 0.13	-14.14 ± 0.14	3.12×10^{-15}	$(4.41 \pm 0.05) \times 10^{-14}$	$-1.01^{+0.02}_{-0.02}$	$1.08^{+0.13}_{-0.13}$	$-6.31^{+0.12}_{-0.12}$
HD 190073	IV B	-24.79 ± 0.50	10.60 ± 0.19	-35.39 ± 0.53	1.99×10^{-15}	$(7.05 \pm 0.11) \times 10^{-14}$	$0.22^{+0.10}_{-0.08}$	$2.31^{+0.18}_{-0.15}$	$-4.97^{+0.18}_{-0.14}$
V1685 Cyg	II B	-107.70 ± 0.67	3.63 ± 0.03	-111.33 ± 0.67	2.63×10^{-15}	$(2.93 \pm 0.02) \times 10^{-13}$	$0.88^{+0.05}_{-0.04}$	$2.97^{+0.15}_{-0.14}$	$-4.77^{+0.09}_{-0.11}$
LkHA 134	I	-68.47 ± 0.36	9.64 ± 0.08	-78.11 ± 0.37	6.45×10^{-16}	$(5.04 \pm 0.02) \times 10^{-14}$	$0.05^{+0.04}_{-0.03}$	$2.14^{+0.10}_{-0.10}$	$-5.28^{+0.11}_{-0.10}$
HD 200775	II R	-66.71 ± 0.23	5.21 ± 0.06	-71.92 ± 0.24	1.36×10^{-14}	$(9.76 \pm 0.04) \times 10^{-13}$	$-1.05^{+0.03}_{-0.03}$	$1.04^{+0.14}_{-0.14}$	$-6.48^{+0.13}_{-0.15}$
LkHA 324	II R	-2.54 ± 0.03	7.74 ± 0.13	-10.28 ± 0.13	7.60×10^{-16}	$(7.81 \pm 0.10) \times 10^{-15}$	-	-	-
HD 203024	I	8.88 ± 0.04	14.42 ± 0.20	-5.54 ± 0.20	8.72×10^{-16}	$(4.83 \pm 0.18) \times 10^{-15}$	-	-	-
V645 Cyg	I	-99.65 ± 1.32	2.15 ± 0.05	-101.80 ± 1.33	4.39×10^{-16}	$(4.47 \pm 0.06) \times 10^{-14}$	-	-	-
V361 Cep	I	-30.74 ± 0.24	5.11 ± 0.06	-35.85 ± 0.25	1.05×10^{-15}	$(3.75 \pm 0.03) \times 10^{-14}$	$-0.03^{+0.04}_{-0.03}$	$2.06^{+0.10}_{-0.10}$	$-5.54^{+0.10}_{-0.10}$
V373 Cep	III B	-55.39 ± 0.39	7.40 ± 0.15	-62.80 ± 0.42	5.10×10^{-16}	$(3.21 \pm 0.02) \times 10^{-14}$	-	-	-
V1578 Cyg	III B	-19.29 ± 0.06	10.30 ± 0.09	-29.59 ± 0.11	7.77×10^{-16}	$(2.30 \pm 0.01) \times 10^{-14}$	$-0.37^{+0.04}_{-0.03}$	$1.72^{+0.11}_{-0.11}$	$-5.67^{+0.10}_{-0.10}$
LkHA 257	I	-5.40 ± 0.00	12.92 ± 0.25	-18.32 ± 0.25	8.56×10^{-17}	$(1.57 \pm 0.02) \times 10^{-15}$	$-1.51^{+0.03}_{-0.02}$	$0.58^{+0.16}_{-0.16}$	$-6.95^{+0.17}_{-0.18}$
SV Cep	III R	2.18 ± 0.16	4.89 ± 0.45	-12.71 ± 0.48	2.08×10^{-16}	$(2.65 \pm 0.10) \times 10^{-15}$	$-2.01^{+0.03}_{-0.03}$	$0.08^{+0.19}_{-0.19}$	$-7.46^{+0.17}_{-0.17}$
V375 Lac	IV B	-18.88 ± 0.21	12.37 ± 0.02	-13.12 ± 0.21	9.02×10^{-17}	$(2.82 \pm 0.02) \times 10^{-15}$	$0.39^{+0.03}_{-0.03}$	$2.48^{+0.12}_{-0.11}$	$-5.17^{+0.10}_{-0.09}$
HD 216629	II B	-17.02 ± 0.09	3.68 ± 0.04	-20.70 ± 0.10	5.84×10^{-15}	$(1.21 \pm 0.01) \times 10^{-13}$	$0.44^{+0.04}_{-0.04}$	$2.53^{+0.13}_{-0.12}$	$-4.95^{+0.11}_{-0.10}$
V374 Cep	II B	-32.95 ± 0.31	4.62 ± 0.05	-37.56 ± 0.31	3.09×10^{-15}	$(1.16 \pm 0.01) \times 10^{-13}$	-	-	-
V628 Cas	IV B	-124.89 ± 2.44	2.10 ± 0.01	-126.99 ± 2.44	6.52×10^{-15}	$(8.28 \pm 0.16) \times 10^{-13}$	-	-	-

study by V18. Adding 85 objects from V18 results in a large sample of 163 H AeBes with mass accretion rates⁴

5 ANALYSIS

We have obtained new spectroscopic data of 30 northern H AeBes, which are used to determine their stellar parameters, extinction, and H α emission line fluxes. Combined with *Gaia* DR2 parallaxes, this led to the determination of the mass accretion rates for 21 of these objects. This dataset complements the large southern sample of F15, for which we re-determined stellar parameters using the *Gaia* parallaxes and extinctions in the same manner as for the northern sample. This full sample contains 78 objects with homogeneously determined values. To this we add 85 objects from the V18 study for which literature values have been adapted and new H α line measurements have been added using data from archives. This led to a total of 163 objects for which we have stellar parameters, distances, H α emission line fluxes and mass accretion rates derived from these using the MA paradigm available. In the following, we will investigate the dependence of the MA-derived accretion rate on stellar mass, and find that there is a break in properties around $4 M_{\odot}$.

5.1 Accretion luminosity as a function of stellar luminosity

Before addressing the mass accretion rate, let us first discuss the accretion luminosity, as that is less dependent on the stellar parameters. In Fig. 6, we show the accretion luminosity versus the stellar luminosity for the entire sample. The accretion luminosity increases monotonically with stellar luminosity, which confirms earlier reports (F15, Mendigutía et al. 2011b). However, the sample under consideration is much larger than previously.

It would appear that the slope decreases, while the scatter in the relationship increases, with mass. To investigate whether there is a significant difference in accretion luminosities between high- and low mass objects, and if so, to determine the mass where there is a turn-over, we split the data into a low-mass and a high-mass sample, with a varying turnover mass. We then fitted a straight line to the data from the lowest mass to this intermediate mass, and a straight line from the intermediate mass to the largest mass. The intermediate mass was varied from the second smallest to the second largest mass.

This resulted in values of the slopes and their statistical uncertainty for a range of masses. When taking the difference in slopes and expressing this in terms of the respective uncertainties in the fit, we arrive at a statistical assessment whether the low- and high-mass samples have a different slope. This approach takes into account the issue that the absolute value of the difference-in-slopes may not be a reliable indicator of the turn-over point. This is because each slope can vary depending on both the number and spread of data points used. For example, at both the high- and low-mass ends, the

⁴When drafting this manuscript, a paper by Arun et al. (2019) was published reporting on the accretion rates using *Gaia* data of a somewhat smaller sample than here. Notable differences are that we use homogeneously determined stellar parameters for a large fraction of the sample and the fact that their sample is not selected for parallax quality and therefore includes faulty *Gaia* parallax measurements affecting the derived distances. It would also appear that their determination of the H α line luminosity does not account for underlying absorption, which will affect especially the weakly emitting sources. As the authors do not provide all relevant datatables, it proved hard to investigate and assess further differences.

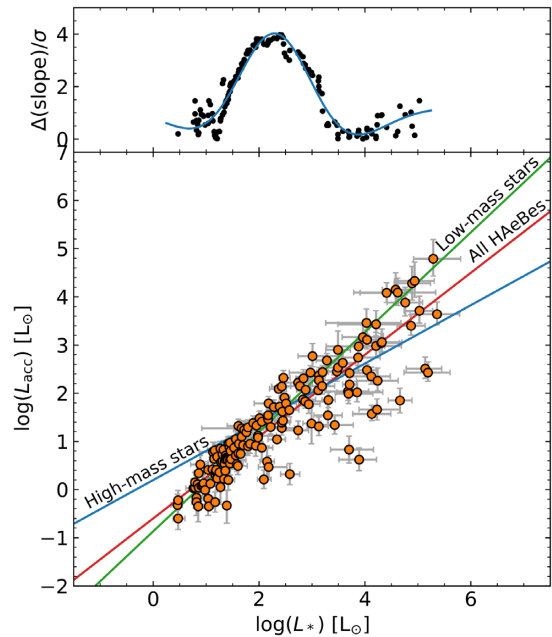


Figure 6. The logarithmic accretion luminosities versus stellar luminosities for the full, 163 stars, sample. Also shown are linear fits to the full sample and to the low- and high-mass stars, respectively. As can be seen in the top panel, the difference in slopes between the low- and high-mass objects is most significant at $L_* > 194 L_{\odot}$ (see text for details). The gradients of best fits for the whole sample, low-mass and high-mass H AeBes are 0.85 ± 0.03 , 1.03 ± 0.08 , and 0.60 ± 0.08 , respectively.

slopes will have a large uncertainty simply because of small number statistics.

We quantify the difference in slopes by combining the uncertainties on both low- and high-mass gradients, σ , and compare this to the difference in slopes, $\Delta(\text{slope})$. This is shown in the top panel of Fig. 6. The $\Delta(\text{slope})$ reaches its maximum significance of 4σ for a luminosity of $194 L_{\odot}$, which was determined by a triple-Gaussian fit to the curve. For the lower mass H AeBes, the linear best fit provides the empirical calibration of $\log(L_{\text{acc}}/L_{\odot}) = (-0.87 \pm 0.11) + (1.03 \pm 0.08) \times \log(L_*/L_{\odot})$. This is in agreement with the best fit for low-mass stars in the work of Mendigutía et al. (2011b) ($L_{\text{acc}} \propto L_*^{1.2}$). For the higher mass H AeBes, the best fit provides the expression of $\log(L_{\text{acc}}/L_{\odot}) = (0.19 \pm 0.27) + (0.60 \pm 0.08) \times \log(L_*/L_{\odot})$.

5.2 Mass accretion rate as a function of stellar mass

One of the main questions regarding the formation of massive stars is at which mass the mass accretion mechanism changes from magnetically controlled accretion to another mechanism, which could be direct accretion from the disc on to the star. Above we saw that there is a difference in the accretion luminosity to stellar luminosity relationships for different masses. So, we now move to look at the mass accretion rates and investigate various subsamples individually.

Let us first consider the sample with homogeneously derived mass accretion rates, before investigating the full sample. The relationship between mass accretion rate and stellar mass of the combined sample from this work and F15, F17 that are present in Thé et al. (1994, table 1), is shown in the left-hand panel of Fig. 7. The sample of Thé et al. (1994), contains the best established H AeBes, and is thus least contaminated by possible misclassified

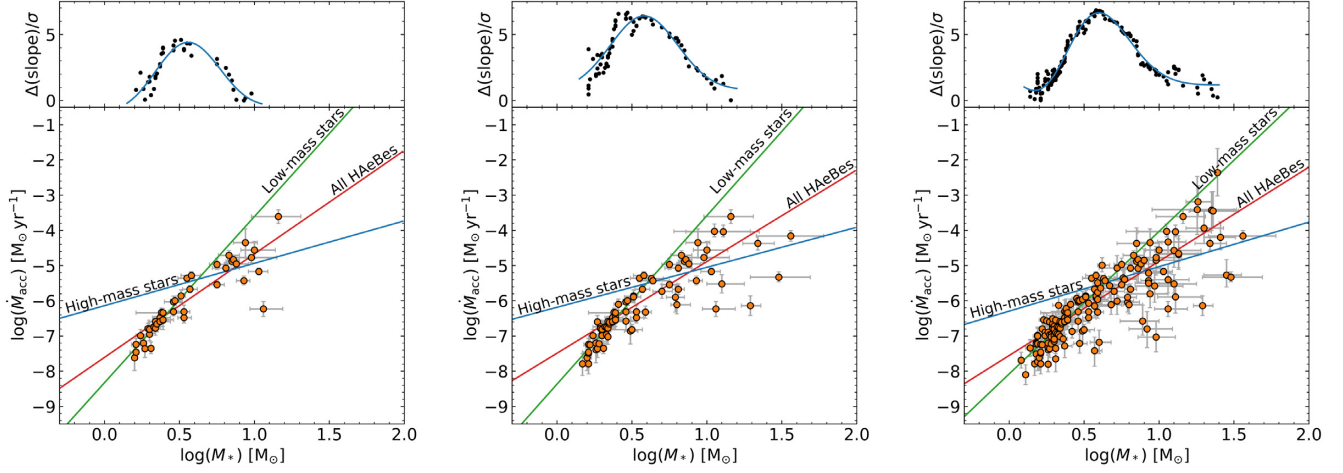


Figure 7. The difference of the gradient of the best fits between the low-mass and the high-mass H AeBs in terms of the uncertainty of the gradient difference (top panel) and the mass accretion rates versus stellar masses (bottom panel). Left: 43 stars from this work sample and the sample of F15 presents in table 1 of Thé et al. (1994). Objects are separated into the low-mass H AeBs, $M_* < 3.61 M_\odot$, and the high-mass H AeBs, $M_* > 3.61 M_\odot$. The slopes of best fits for the whole sample, low-mass and high-mass H AeBs are 2.94 ± 0.24 , 4.72 ± 0.49 , and 1.20 ± 0.65 , respectively. Middle: 78 objects from this work sample and the sample of F15. The break is defined at $M_* = 3.81 M_\odot$. The gradients of best fits for the whole sample, low-mass and high-mass H AeBs are 2.60 ± 0.19 , 4.78 ± 0.34 , and 1.14 ± 0.46 , respectively. Right: 163 objects are separated into the low-mass H AeBs and the high-mass H AeBs at $M_* = 3.98 M_\odot$. The gradients of best fits for the whole sample, low-mass and high-mass H AeBs are 2.67 ± 0.13 , 4.05 ± 0.24 , and 1.26 ± 0.34 , respectively.

objects. It can be seen that the mass accretion rate increases with stellar mass, and that there is a different behaviour for objects with masses below and above the mass range with $\log(M_*) = 0.4\text{--}0.6$. This break is consistent with the major finding in F15 that the relationship between mass accretion rate and stellar mass shows a break around the boundary between Herbig Ae and Herbig Be stars. In particular, they found that the relationship between mass accretion rate and mass has a different slope for the lower and higher mass objects, respectively. With our improved sample in hand, we can now revisit this finding and we determine the mass at which the break occurs with higher precision in the same way as we found the turnover luminosity earlier.

We found that the maximum slope difference is at the 4.4σ level for the Thé et al. sample at $\log(M_*) = 0.56^{+0.14}_{-0.14}$ or $M_* = 3.61^{+1.38}_{-0.98} M_\odot$. The uncertainty in the mass is decided where the difference in slope is 1σ smaller than at maximum. If we focus on the total combined sample of 78 objects from this work and F15, the break is established at $\log(M_*) = 0.58^{+0.14}_{-0.14}$ or $M_* = 3.81^{+1.46}_{-1.05} M_\odot$ with the maximum gradient difference about 6.4σ , as shown in the middle panel of Fig. 7. It can be seen that this plot shows the same relationship as the one in the left-hand panel. When considering the full, combined sample of 163 objects from this work, F15 and V18 whose mass accretion rates are shown in the right-hand panel of Fig. 7, the break is now found at the $\log(M_*) = 0.60^{+0.13}_{-0.12}$ or $M_* = 3.98^{+1.37}_{-0.94} M_\odot$ with the maximum difference of gradient about 6.6σ .

We note that both the significance of the difference in slopes as well as the mass at which the break occurs increases with the number of objects. This could be due to the number of objects; especially as the Thé et al. (1994) sample is sparsely populated at the high-mass end, which could increase the uncertainty on the resulting slope and thus lower the significance of the difference in slopes between high- and low-mass objects. Alternatively, it could be affected by a larger contamination of non-Herbig Be stars in the full sample. It is notoriously hard to differentiate between a regular Be star and a Herbig Be star. Given the low number statistics of the Thé et al.

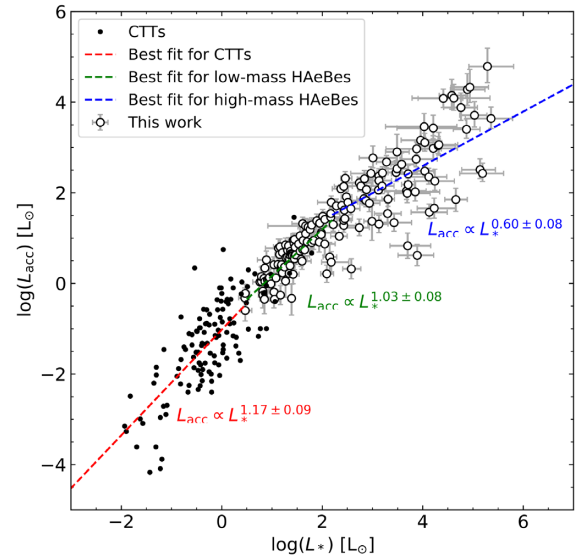


Figure 8. Accretion luminosity versus stellar luminosity for 163 H AeBs in this work and classical T Tauri stars from Hartmann et al. (1998), White & Basri (2003), Calvet et al. (2004), and Natta et al. (2006). Red, green, and blue dashed lines are the best fit for T Tauri stars ($L_{\text{acc}} \propto L_*^{1.17 \pm 0.09}$), low-mass H AeBs ($L_{\text{acc}} \propto L_*^{1.03 \pm 0.08}$) and high-mass H AeBs ($L_{\text{acc}} \propto L_*^{0.60 \pm 0.08}$), respectively.

(1994) sample and the similarity of the break in mass of the other two samples, we will proceed with a break in slope at $4 M_\odot$.

5.2.1 Literature comparisons with T Tauri stars

It is interesting to see how the accretion luminosities compare to those of T Tauri stars at the low mass range. With the large caveat that no *Gaia* DR2 study of T Tauri stars and their stellar parameters and accretion rates exists at the moment, we show in Fig. 8 the

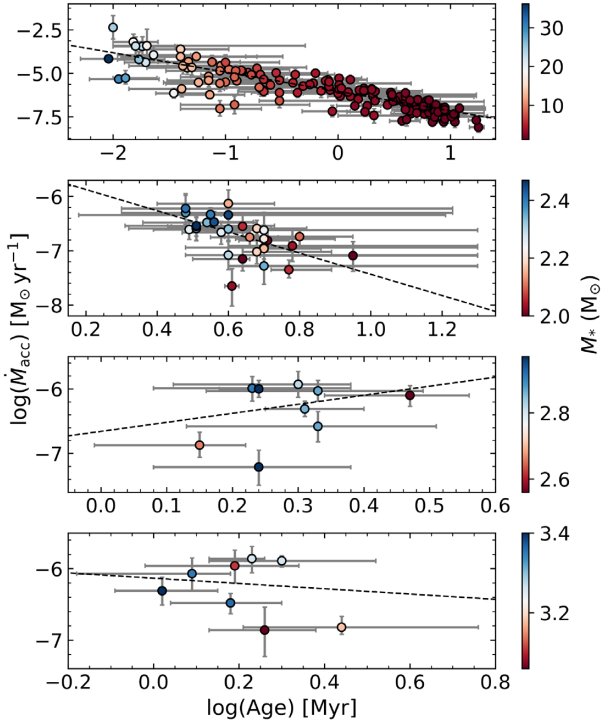


Figure 9. Ages versus mass accretion rates. From top to bottom all sample, the mass range $2.0\text{--}2.5 M_{\odot}$, $2.5\text{--}3.0 M_{\odot}$, and $3.0\text{--}3.5 M_{\odot}$. The best fit is shown in the dashed line where $\dot{M}_{\text{acc}} \propto \text{Age}^{-1.11 \pm 0.05}$, $\dot{M}_{\text{acc}} \propto \text{Age}^{-1.95 \pm 0.49}$, $\dot{M}_{\text{acc}} \propto \text{Age}^{1.40 \pm 1.47}$, and $\dot{M}_{\text{acc}} \propto \text{Age}^{-0.37 \pm 1.25}$, respectively. The colour map indicates stellar mass of each mass bin.

L_{acc} against L_* for the whole sample of 163 H AeBes in this work compared to classical T Tauri stars of which all luminosity values are taken from Hartmann et al. (1998), White & Basri (2003), Calvet et al. (2004), and Natta, Testi & Randich (2006). On one hand, the gradient of best fit for the classical T Tauri stars is 1.17 ± 0.09 which is close, and well within the errorbars, to 1.03 ± 0.08 for low-mass H AeBes. On the other hand, high-mass H AeBes shows a flatter relationship of $L_{\text{acc}} \propto L_*^{0.60 \pm 0.08}$. It would seem that the Herbig Ae and Be stars with masses up until $4 M_{\odot}$ behave similarly to the T Tauri stars. Again, stellar parameters of these classical T Tauri stars were not derived in the same manner as H AeBes in this work. This may have an effect on our conclusion.

5.3 Mass accretion rate as a function of stellar age

In Fig. 5, we illustrate the mass accretion rates across the HR-diagram. As expected, it can be seen that the accretion rates are largest for the brightest and most massive objects. However, the sample may allow an investigation into the evolution of the mass accretion rate as a function of stellar age as provided by the evolutionary models. In general, it can be stated that, in terms of evolutionary age, the younger objects have higher accretion rates than older objects. As illustration, we show the mass accretion rate as a function of age in the top panel of Fig. 9. It is clear that the accretion rate decreases with age (as also shown in F15); the Pearson correlation coefficient is -0.87 .

However, when considering any properties as a function of age, there is always the issue that higher mass stars evolve faster than lower mass stars. Hence, the observed fact that higher mass objects have higher accretion rates could be the main underlying reason

for a trend of decreasing accretion rate with time. Indeed, in the top panel of Fig. 9 the range in accretion rates covers the entire accretion range of the accretion versus mass relation, so it is hard to disentangle from this graph whether there is also an accretion rate – age relation.

This can, in principle, be circumvented when selecting a sample of objects in a small mass range, so that the spread in mass accretion rates is minimized. This needs to be offset against the number of objects under consideration. In the lower panels of Fig. 9, we show how the accretion rate change with the age of stars in three different mass bins ($2.0\text{--}2.5 M_{\odot}$, $2.5\text{--}3.0 M_{\odot}$, and $3.0\text{--}3.5 M_{\odot}$). A best fit taken into account the uncertainties in both the mass accretion rate and age to the 30 objects where $2.0 M_{\odot} < M_* < 2.5 M_{\odot}$ shows a $\dot{M}_{\text{acc}} \propto \text{Age}^{-1.95 \pm 0.49}$ with a Pearson’s correlation coefficient -0.55 . The nine stars with masses $2.5 M_{\odot} < M_* < 3.0 M_{\odot}$ have a gradient of a best fit is -1.40 ± 1.47 (correlation coefficient 0.40). The error of the best-fitting gradient becomes slightly larger than its own value, which is due to the smaller number of objects involved. The eight objects with $3.0 M_{\odot} < M_* < 3.5 M_{\odot}$ in the bottom panel of Fig. 9 have a gradient of a best fit is -0.37 ± 1.25 with a linear correlation -0.36 . It can be seen that the error of the best fit gets larger than three times of its own absolute value. This is more likely to be due to the lack of H AeBes when the stellar mass increases.

The $2.0\text{--}2.5 M_{\odot}$ sample is best suited to study any trend in accretion rate with age in the sense that the accretion rates change by 0.4 dex across this mass range (cf. the slope of 4.05 found for the low mass objects in Section 5.2). The spread in accretion rates in the graph is twice that, and if the additional decrease in mass accretion rate is due to evolution, we find $\dot{M}_{\text{acc}} \propto \text{Age}^{-1.95 \pm 0.49}$. This value is the only such determination for H AeBes in a narrow mass range, other determinations were based on full samples of H AeBe stars which contain many different masses and suffer from a mass-age degeneracy (e.g. F15, Mendigutía et al. (2012)). Despite the relatively large errorbars, we note that our determination is remarkably close to the observed values for T Tauri stars by Hartmann et al. (1998), who find an η between 1.5–2.8, while theoretically these authors predict η to be larger than 1.5 for a single α viscous disc. We also refer the reader to the discussion in Mendigutía et al. (2012), who, remarkably, find a similar value of the exponent to ours: $1.8_{-0.7}^{+1.4}$ as determined for their full sample.

6 DISCUSSION

In the above, we have worked out the mass accretion rates for a large sample of 163 H AeBes. To this end new and spectroscopic archival data were employed. A large fraction of the sample now has homogeneously determined astrophysical parameters, while *Gaia* parallaxes were used to arrive at updated luminosities for the sample objects. We compared the mass accretion rates derived using the MA paradigm for H AeBes with various properties. We find that:

- (i) The mass accretion rate increases with stellar mass, but the sample can be split into two subsets depending on their masses.
- (ii) The low-mass Herbig Ae stars’ accretion rates have a steeper dependence on mass than the higher mass Herbig Be stars.
- (iii) The above findings corroborate previous reports in the literature. The larger sample and improved data allows us to determine the mass where the largest difference in slopes between high- and low-mass objects occurs. We find it is $4 M_{\odot}$.
- (iv) Bearing in mind the caveat that T Tauri stars do not yet have *Gaia* based accretion rates, it appears that the Herbig Ae stars’

accretion properties display a similar dependence on luminosity as the T Tauri stars.

(v) In general, younger objects have larger mass accretion rates, but it proves not trivial to disentangle a mass dependence from an age dependence. We present the first attempt to do so. A small subset in a narrow mass range leads us to suggest that the accretion rate decreases with time.

In the following, we aim to put these results into context, but we start by discussing the various assumptions that had to be made to arrive at these results.

6.1 On the viability of the MA model to determine accretion rates of HAeBes

In the above, we have determined accretion luminosities and accretion rates to young stars. However, the question remains whether the magnetic accretion shock modelling that underpins these computations should be applicable. After all, A and B-type stars typically do not have magnetic field detections, and indeed, are not expected to harbour magnetic fields as their radiative envelopes would not create a dynamo that, in turn, can create a magnetic field. This was verified in a study of Intermediate Mass T Tauri stars (IMTTS) by Villebrun et al. (2019) who found that the fraction of PMS objects with a magnetic field detection drops markedly as they become hotter (for similar masses). These authors suspect that any B-field detections in HAeBes could be fossil fields from the evolutionary stage immediately preceding them. The fields would not only be weaker, but also more complex, hampering their direct detection.

Muzerolle et al. (2004) showed that the MA models provided qualitative agreement with the observed emission line profiles of the Herbig Ae star UX Ori. In the process, they also found that the B-field geometry should be more complex than the usual dipole field in T Tauri stars and the expected field strength would be much below the usual T Tauri detections, in line with the Villebrun et al. (2019) findings.

Since, based on statistical studies and targeted individual investigations evidence has emerged that Herbig Ae stars are similar to the T Tauri stars. Garcia Lopez et al. (2006) showed that the accretion rate properties of the Herbig Ae stars constitute a natural extension to the T Tauri stars, while F15 demonstrated that the MA model can reproduce the observed UV excesses towards most of their HAeBes with realistic parameters for the shocked regions. A small number of objects, all Herbig Be stars, could not be explained with the MA model. They exhibit such a large UV-excess that they would require shock covering factors larger than 100 per cent, which is clearly unphysical.

Vink et al. (2002) and Vink et al. (2005) were the first to point out the remarkable similarity in the observed linear spectropolarimetric properties of the H α line in Herbig Ae stars and T Tauri stars. The polarimetric line effects in these types of objects can be explained with geometries consistent with light scattering off (magnetically) truncated discs. In contrast, the very different effects observed towards the Herbig Be stars were more consistent with discs reaching on to the central star – hinting at a different accretion mechanism in those. The large sample by Ababakr et al. (2017) allowed them to identify the transition region to be around spectral type B7/8.

Cauley & Johns-Krull (2014) studied the He I 1.083 μm line profiles of a large sample of Herbig stars and found that both T Tauri and Herbig Ae stars could be explained with MA, while the Herbig

Be stars could not. Reiter et al. (2018) did not detect a difference in line morphology between the few (5) magnetic HAeBes and the rest of the sample. They argued that Herbig Ae stars may therefore not accrete similarly to T Tauri stars. However, based on Poisson statistics alone, even if all magnetic objects showed either a P Cygni or Inverse P Cygni profile, a sample of five would not be sufficient to conclusively demonstrate that the magnetic objects are, or are not, different from the non-magnetic objects. Clearly, more work needs to be done in this area. Costigan et al. (2014) investigated the H α line variability properties of HAeBes and T Tauri stars and found that both the time-scales and amplitude of the variability were similar for the Herbig Ae and T Tauri, which also led these authors to suggest that the mode of accretion of these objects are similar. A notion also implied by our result in Fig. 8 that the accretion luminosities of both Herbig Ae and T Tauri stars appear to have the same dependence on the stellar luminosity. Finally, Mendigutía et al. (2011a) found that the H α line width variability of Herbig Be stars is considerably smaller than for Herbig Ae stars, which is, in turn, smaller than for TTs (see fig. 37 in Fang et al. 2013). This may suggest smaller line emitting regions/magnetospheres as the stellar mass increases, and thus a eventual transition from MA to some other mechanism responsible for accretion.

To summarize this section, various studies of different observational properties have confirmed the many similarities between T Tauri and Herbig Ae stars, which in turn hint at a similar accretion mechanism, the magnetically controlled accretion. In turn, this would validate our use of the MA shock modelling to derive mass accretion rates for at least the lower mass end of the Herbig Ae/Be star range. Before we discuss the accretion mechanisms for low- and high-mass stars, we address the use of line luminosities to arrive at accretion luminosities and rates below.

6.2 On the use of line emission as accretion rate diagnostic

The only ‘direct’ manner to determine the mass accretion rate is to measure the accretion luminosity, which is essentially the amount of gravitational potential energy that is converted into radiation at ultraviolet wavelengths. This can then be turned into a mass accretion rate once the stellar mass and radius are known. The determination of the contribution of the accretion shock to the total UV emission for HAeBe objects is not straightforward due to the fact that these stars intrinsically emit many UV photons by virtue of their higher temperatures.

Calvet et al. (2004) showed that the Br γ emission strengths observed towards a sample of IMTTS correlated with the accretion luminosity as determined by the UV excess for a large mass range extending to 3.7 M_{\odot} (the mass of their most massive target, GW Ori, with spectral type G0 – cool enough to unambiguously determine the UV excess emission). This was already known for lower mass objects, but, significantly, these authors extended it to higher masses. In addition, these authors also showed that the mass accretion rate correlated with the stellar mass over this mass range. Therefore they also demonstrated that line emission, in this case the hydrogen recombination Br γ , can be used to measure accretion rates to masses of at least up to $\sim 4 M_{\odot}$. Mendigutía et al. (2011b) measured the UV-excess of HAeBes using UV-blue spectroscopy and photometry, respectively, and noted the correlation with emission line strengths (see also Donehew & Brittain 2011). F15 and F17 took this further and demonstrated the strong correlation between emission line strength and accretion luminosity for a much larger sample and a mass range going up to 10–15 M_{\odot} . It extended to an accretion

luminosity of $10^4 L_{\odot}$ and was shown to hold for a large number of different emission lines.

One should keep in mind the caveat, also pointed out by F17, that high spatial resolution optical and near-IR studies of the hydrogen line emission do not necessarily identify the line emitting regions of HAeBes with the magnetospheric accretion channels. Already in 2008, Kraus et al. (2008) reported that their milli-arcsec resolution AMBER interferometric data indicated different Br γ line forming regions which were consistent with the MA scenario for some objects but with disc-winds for others. Further studies by e.g. Mendigutía et al. (2015b) find the line emission region consistent with a rotating disc. Similarly, Tambovtseva, Grinin & Weigelt (2016) and Kreplin et al. (2018) find the disc-wind a more likely explanation for the emitting region than the compact accretion channels. Even higher resolution H α CHARA data discussed by Mendigutía et al. (2017) present a similar diversity.

There thus remains the question whether we can use emission lines to probe accretion if they are apparently not related to the accretion process itself, or indeed, why the line luminosities correlate with the accretion luminosity at all. It is well known that accretion on to young stars drives jets and outflows, where the mass ejection rates are of order 10 per cent of the accretion rates (see e.g. Purser et al. 2016). If this is also the case for HAeBes, then one could expect the emission lines to be correlated with the accretion rates. On the other hand, Mendigutía et al. (2015a) pointed out that while the physical origin of the lines may not be related to the accretion process *per se*, it is the underlying correlation between accretion luminosity and stellar luminosity that gives rise to a correlation between the line strengths and accretion. Hence, although the lines may not necessarily be directly accretion-related, the empirical correlations between emission line luminosities and accretion luminosities are strong enough to validate their use as accretion tracers.

When we revisit the various studies mentioned above, it is notable that a distinction between Herbig Ae and Herbig Be stars is found, spectroscopically (Cauley & Johns-Krull 2014), spectropolarimetrically (Vink et al. 2005), due to spectral variability (Costigan et al. 2014), and even when considering the accretion rates from UV-excesses (F15).

Based on the break in accretion rates, we can move this boundary to a critical mass of $4M_{\odot}$, remarkably close, but not perfectly so, to the boundary of around B7/8 put forward by Ababakr et al. (2017). It is thus implied that there is a transition from magnetically controlled accretion in low-mass HAeBes to another accretion mechanism in high-mass HAeBes at around $4M_{\odot}$. The remaining question is what this mechanism should be.

6.3 If MA does not operate in massive objects, what then?

The spectropolarimetric finding of a disc reaching on to the star is reminiscent of the Boundary Layer (BL) accretion mechanism that was found to be a natural consequence of a viscous circumstellar disc around a stellar object (Lynden-Bell & Pringle 1974). The BL is a thin annulus close to the star in which the material reduces its (Keplerian) velocity to the slow rotation of the star when it reaches the stellar surface. It is here that kinetic energy and angular momentum will be dissipated. The BL mechanism was originally used to explain the observed UV excesses of low mass PMS stars (Bertout, Basri & Bouvier 1988) until observations led to strong support for the magnetic accretion scenario instead (Bouvier et al. 2007). One of the difficulties the BL mechanism had was the smaller redshifted absorption linewidths predicted from the

Keplerian widths expected from the BL than from freefall in the case of MA (Bertout et al. 1988). It had been suggested in the past to operate in Herbig Ae/Be objects (eg Blondel & Djie 2006 who studied Herbig Ae stars; Mendigutía et al. 2011b; Cauley & Johns-Krull 2014) but has never been adapted and tested for masses of Herbig Be stars and greater.

It is very much beyond the scope of this paper to address the BL theoretically, but let us suffice with a basic consideration to see whether we would be able to expect a different slope in the derived accretion rate or luminosity for an object undergoing MA or BL accretion. In both situations infalling material converts energy into radiation. In MA the energy released by a mass dM falling on to a star with mass and radius M_* and R_* respectively will be the gravitational potential energy of the infalling material, $\frac{GM_*dM}{R_*}$, times a factor close to 1 accounting for the fact that material is not falling from infinity.

How would this amount of released energy compare to that in the BL scenario for infalling material of the same mass dM ? For the BL case, the accretion energy will be at most the kinetic energy of the rotating material prior to being decelerated in the very thin layer close to the stellar surface. As the material rotates Keplerian, we know that the centripetal force equals the force of gravity, $\frac{dMv^2}{R_*} = \frac{GM_*dM}{R_*^2}$. We thus find that the kinetic energy $\frac{1}{2}dMv^2 = \frac{GM_*dM}{2R_*}$, which is half the gravitational potential energy for the same mass.

In other words, the energy released in the BL scenario will be *less* than that released by MA for the same mass. Therefore if the mass accretion rate is the same, we obtain a lower accretion luminosity for objects accreting material through a BL than through Magnetospheric Accretion. This also means that the accretion rate has to be larger in BL to arrive at the same accretion luminosity. In turn, this has as implication that if we derive the mass accretion rates using the MA paradigm, while the accretion is due to BL, then the resulting accretion luminosities and rates would have been underestimated.

Earlier, we found that the (MA derived) accretion luminosities have the same dependence of the accretion luminosity on the stellar luminosity for T Tauri stars and Herbig Ae stars, while we find a smaller gradient for the more massive stars. If we would assume that this dependence would hold for more massive stars too, then it could be concluded that the accretion rates have been underestimated for massive Herbig Be stars. If the BL scenario was the acting mechanism for the Herbig Be stars then the accretion luminosities would be larger - possibly resulting in the same relationship between accretion and stellar luminosity as the lower mass stars, and no break would be visible.

Could that be the case here? The accretion on to the stars likely depends on the rates the accretion discs are fed and mass needs to be transported through the disc, so it may be reasonable to assume that this process is less dependent on the stellar parameters and a simple correlation between accretion on to the star and stellar luminosity (or mass) would be expected. It is intriguing that the BL scenario for more massive stars might explain why we obtain lower accretion rates when we assume MA for the more massive objects resulting in a break at around $4M_{\odot}$. An in-depth investigation into the BL is certainly warranted.

7 FINAL REMARKS

In this paper, we presented an analysis of a new set of optical spectroscopy of 30 northern HAeBes. This was combined with our data and analysis of southern objects in F15 resulting in a set of temperatures, gravities, extinctions, and luminosities that were

derived in a consistent manner. As such this constitutes the largest homogeneously analysed sample of 78 HAeBes to date. To these we added 85 objects from the *Gaia* DR2 study of V18. The total sample of 163 objects allowed us to derive the accretion luminosities and mass accretion rates using the empirical power-law relationship between accretion luminosity and line luminosity as derived under the MA paradigm.

We identified a subset in the total sample as being the strongest Herbig Ae/Be star candidates known. The set contains 60 per cent of the objects in Table 1 from the Thé et al. (1994) catalogue. All trends found in the large sample are also present in this subsample. This implies that the large sample likely has a low contamination and is therefore a good representation of the Herbig Ae/Be class.

(i) We find that the mass accretion rate increases with stellar mass, and that the lower mass Herbig Ae stars' accretion rates have a steeper dependence on mass than the higher mass Herbig Be stars. This confirms previous findings, but the large sample allows us to determine the mass where this break occurs. This is found to be $4 M_{\odot}$.

(ii) A comparison of accretion luminosities of the HAeBes with those of T Tauri stars from the literature indicates that the Herbig Ae stars' accretion rates display a similar dependence on luminosity as the T Tauri stars. This provides further evidence that Herbig Ae stars may accrete in a similar fashion as the T Tauri stars. We do caution however that T Tauri stars do not yet have *Gaia*-based accretion rates.

(iii) We also find that in general, younger objects have larger mass accretion rates. However, it is not trivial to disentangle a mass and age dependence from each other: More massive stars have larger accretion rates, but have much smaller ages as well. A small subset selected in a narrow mass range leads us to suggest that the accretion rate does indeed decrease with time. The best value could be determined for the mass range $2.0\text{--}2.5 M_{\odot}$. We find $\dot{M}_{\text{acc}} \propto \text{Age}^{-1.95 \pm 0.49}$.

Finally, we discussed the similarities and differences between the accretion properties of lower mass and higher mass Herbig PMS stars. In particular, we discuss the various lines of evidence that suggest they accrete in different fashions. In addition, from linear spectropolarimetric studies, the Herbig Be stars are found to have discs reaching on to the stellar surface while the Herbig Ae stars (with the break around $4 M_{\odot}$) have discs with inner holes, similar to the T Tauri stars.

We therefore put forward the BL mechanism as a viable manner for the accretion on to the stellar surface of massive PMS stars. More work needs to be done, but an initial, crude, estimate of the accretion luminosity dependence on mass – assuming a global correlation between mass accretion rate and stellar mass for all masses – can explain the observed break in accretion properties.

ACKNOWLEDGEMENTS

The authors would like to thank to the anonymous reviewer who provided constructive comments which helped improve the manuscript. CW thanks Thammasat University for financial support in the form of a PhD scholarship at the University of Leeds. IM acknowledges the funds from a 'Talento' Fellowship (2016-T1/TIC-1890, Government of Comunidad Autónoma de Madrid, Spain). MV was funded through the STARRY project which received funding from the European Union's Horizon 2020 research and innovation programme under MSCA ITN-EID grant agreement No 676036. This work has made use of data from the European Space Agency (ESA) mission *Gaia* (<https://www.cosmos.esa.int/gaia>), processed by the

Gaia Data Processing and Analysis Consortium (DPAC, <https://www.cosmos.esa.int/web/gaia/dpac/consortium>). Funding for the DPAC has been provided by national institutions, in particular, the institutions participating in the *Gaia* Multilateral Agreement. This research has made use of IRAF which is distributed by the National Optical Astronomy Observatory, which is operated by the Association of Universities for Research in Astronomy (AURA) under a cooperative agreement with the National Science Foundation. This publication has made use of SIMBAD data base, operated at CDS, Strasbourg, France. It has also made use of NASA's Astrophysics Data System and the services of the ESO Science Archive Facility. Based on observations collected at the European Southern Observatory under ESO programmes 60.A-9022(C), 073.D-0609(A), 075.D-0177(A), 076.B-0055(A), 082.A-9011(A), 082.C-0831(A), 082.D-0061(A), 083.A-9013(A), 084.A-9016(A) and 085.A-9027(B). This research was made possible through the use of the AAVSO Photometric All-Sky Survey (APASS), funded by the Robert Martin Ayers Sciences Fund and NSF AST-1412587.

REFERENCES

- Ababakr K. M., Oudmaijer R. D., Vink J. S., 2017, *MNRAS*, 472, 854
 Alecian E. et al., 2013, *MNRAS*, 429, 1001
 Arun R., Mathew B., Manoj P., Ujjwal K., Kartha S. S., Viswanath G., Narang M., Paul K. T., 2019, *AJ*, 157, 159
 Bertout C., Basri G., Bouvier J., 1988, *ApJ*, 330, 350
 Bessell M. S., 1979, *PASP*, 91, 589
 Blondel P. F. C., Djie H. R. E. T. A., 2006, *A&A*, 456, 1045
 Bohlin R. C., Mészáros S., Fleming S. W., Gordon K. D., Koekemoer A. M., Kovács J., 2017, *AJ*, 153, 234
 Bouvier J., Alencar S. H. P., Harries T. J., Johns-Krull C. M., Romanova M. M., 2007, *Protostars and Planets V*, University of Arizona Press, Chicago, p. 479
 Bressan A., Marigo P., Girardi L., Salasnich B., Dal Cero C., Rubele S., Nanni A., 2012, *MNRAS*, 427, 127
 Calvet N., Cohen M., 1978, *MNRAS*, 182, 687
 Calvet N., Muzerolle J., Briceño C., Hernández J., Hartmann L., Saucedo J. L., Gordon K. D., 2004, *AJ*, 128, 1294
 Cardelli J. A., Clayton G. C., Mathis J. S., 1989, *ApJ*, 345, 245
 Catala C. et al., 2007, *A&A*, 462, 293
 Cauley P. W., Johns-Krull C. M., 2014, *ApJ*, 797, 112
 Clarke A. J., Lumsden S. L., Oudmaijer R. D., Busfield A. L., Hoare M. G., Moore T. J. T., Sheret T. L., Urquhart J. S., 2006, *A&A*, 457, 183
 Costigan G., Vink J. S., Scholz A., Ray T., Testi L., 2014, *MNRAS*, 440, 3444
 Dahm S. E., Hillenbrand L. A., 2015, *AJ*, 149, 200
 De Winter D., van den Ancker M. E., Maira A., Thé P. S., Djie H. R. E. T. A., Redondo I., Eiroa C., Molster F. J., 2001, *A&A*, 380, 609
 Donehew B., Brittain S., 2011, *AJ*, 141, 46
 Fairlamb J. R., Oudmaijer R. D., Mendigutía I., Ilee J. D., van den Ancker M. E., 2015, *MNRAS*, 453, 976(F15)
 Fairlamb J. R., Oudmaijer R. D., Mendigutía I., Ilee J. D., van den Ancker M. E., 2017, *MNRAS*, 464, 4721(F17)
 Fang M., Kim J. S., van Boekel R., Sicilia-Aguilar A., Henning T., Flaherty K., 2013, *ApJS*, 207, 5
 Fernandez M., 1995, *A&AS*, 113, 473
 Gaia Collaboration et al., 2016, *A&A*, 595, A2
 Gaia Collaboration et al., 2018, *A&A*, 616, A1
 Garcia Lopez R., Natta A., Testi L., Habart E., 2006, *A&A*, 459, 837
 Garrison R. F., 1970, *AJ*, 75, 1001
 Hamann F., Persson S. E., 1992, *ApJS*, 82, 285
 Hartmann L., Calvet N., Gullbring E., D'Alessio P., 1998, *ApJ*, 495, 385
 Hartmann L., Herczeg G., Calvet N., 2016, *ARA&A*, 54, 135
 Herbig G. H., 1958, *ApJ*, 128, 259
 Herbig G. H., 1960, *ApJS*, 4, 337
 Herbst W., Shevchenko V. S., 1999, *AJ*, 118, 1043

- Hernández J., Calvet N., Briceño C., Hartmann L., Berlind P., 2004, *AJ*, 127, 1
- Hillenbrand L. A., Strom S. E., Vrba F. J., Keene J., 1992, *ApJ*, 397, 613
- Ingleby L. et al., 2013, *ApJ*, 767, 112
- Kahn F. D., 1974, *A&A*, 37, 149
- Kraus S. et al., 2008, *A&A*, 489, 1157
- Kreplin A., Tarnopolska L., Grinin V., Kraus S., Weigelt G., Wang Y., 2018, *MNRAS*, 476, 4520
- Kurucz R., 1993, ATLAS9 Stellar Atmosphere Programs and 2 km/s grid. Kurucz CD-ROM No. 13. Smithsonian Astrophysical Observatory, Cambridge, MA, p. 13
- Lumsden S. L., Hoare M. G., Urquhart J. S., Oudmaijer R. D., Davies B., Mottram J. C., Cooper H. D. B., Moore T. J. T., 2013, *ApJS*, 208, 11
- Lynden-Bell D., Pringle J. E., 1974, *MNRAS*, 168, 603
- Marigo P. et al., 2017, *ApJ*, 835, 77
- Meeus G., Waters L. B. F. M., Bouwman J., van den Ancker M. E., Waelkens C., Malfait K., 2001, *A&A*, 365, 476
- Mendigutía I., Eiroa C., Montesinos B., Mora A., Oudmaijer R. D., Merín B., Meeus G., 2011a, *A&A*, 529, A34
- Mendigutía I., Calvet N., Montesinos B., Mora A., Muzerolle J., Eiroa C., Oudmaijer R. D., Merín B., 2011b, *A&A*, 535, A99
- Mendigutía I., Mora A., Montesinos B., Eiroa C., Meeus G., Merín B., Oudmaijer R. D., 2012, *A&A*, 543, A59
- Mendigutía I., Oudmaijer R. D., Rigliaco E., Fairlamb J. R., Calvet N., Muzerolle J., Cunningham N., Lumsden S. L., 2015a, *MNRAS*, 452, 2837
- Mendigutía I., de Wit W. J., Oudmaijer R. D., Fairlamb J. R., Carciofi A. C., Ilee J. D., Vieira R. G., 2015b, *MNRAS*, 453, 2126
- Mendigutía I., Oudmaijer R. D., Mourard D., Muzerolle J., 2017, *MNRAS*, 464, 1984
- Mészáros S. et al., 2012, *AJ*, 144, 120
- Mora A. et al., 2001, *A&A*, 378, 116
- Muzerolle J., D'Alessio P., Calvet N., Hartmann L., 2004, *ApJ*, 617, 406
- Natta A., Testi L., Randich S., 2006, *A&A*, 452, 245
- Oudmaijer R. D. et al., 2001, *A&A*, 379, 564
- Palla F., Stahler S. W., 1993, *ApJ*, 418, 414
- Purser S. J. D. et al., 2016, *MNRAS*, 460, 1039
- Reipurth B., Pedrosa A., Lago M. T. V. T., 1996, *A&AS*, 120, 229
- Reiter M. et al., 2018, *ApJ*, 852, 5
- Salpeter E. E., 1955, *ApJ*, 121, 161
- Schöller M. et al., 2016, *A&A*, 592, A50
- Skiff B. A., 2014, *VizieR Online Data Catalogue*, 1, 2023
- Smith J. A. et al., 2002, *AJ*, 123, 2121
- Straižys V., Kuriliene G., 1981, *Ap&SS*, 80, 353
- Tarnopolska L., Grinin V. P., Weigelt G., 2016, *A&A*, 590, A97
- Tang J., Bressan A., Rosenfield P., Slemmer A., Marigo P., Girardi L., Bianchi L., 2014, *MNRAS*, 445, 4287
- Thé P. S., de Winter D., Pérez M. R., 1994, *A&AS*, 104, 315
- Van den Ancker M. E., Bouwman J., Wesselius P. R., Waters L. B. F. M., Dougherty S. M., van Dishoeck E. F., 2000, *A&A*, 357, 325
- Vieira S. L. A., Corradi W. J. B., Alencar S. H. P., Mendes L. T. S., Torres C. A. O., Quast G. R., Guimarães M. M., da Silva L., 2003, *AJ*, 126, 2971
- Villebrun F. et al., 2019, *A&A*, 622, A72
- Vink J. S., Drew J. E., Harries T. J., Oudmaijer R. D., 2002, *MNRAS*, 337, 356
- Vink J. S., Drew J. E., Harries T. J., Oudmaijer R. D., Unruh Y., 2005, *MNRAS*, 359, 1049
- Vioque M., Oudmaijer R. D., Baines D., Mendigutía I., Pérez-Martínez R., 2018, *A&A*, 620, A128(V18)
- Walker M. F., 1959, *ApJ*, 130, 57
- White R. J., Basri G., 2003, *ApJ*, 582, 1109
- Wolf B., Stahl O., 1985, *A&A*, 148, 412
- Zacharias N., Finch C. T., Girard T. M., Henden A., Bartlett J. L., Monet D. G., Zacharias M. I., 2013, *AJ*, 145, 44

SUPPORTING INFORMATION

Supplementary appendices are available for download alongside this article on the MNRAS website (<https://academic.oup.com/mnr> as).

Table A1. Log of observations of standard stars.

Fig. B1 The H α line profiles for the 30 objects listed in Table 1.

Table C1. Stellar parameters of 91 HAeBes in the F15 sample.

Table C2. The equivalent width measurements and accretion rates of 91 HAeBes in the F15 sample.

Table D1. The equivalent width measurements and accretion rates of 144 HAeBes in the Vioque et al. (2018) sample.

Please note: Oxford University Press is not responsible for the content or functionality of any supporting materials supplied by the authors. Any queries (other than missing material) should be directed to the corresponding author for the article.

This paper has been typeset from a \LaTeX file prepared by the author.